A&A, 709, A124 (2026)
https://doi.org/10.1051/0004-6361/202658852

Astronomy & Astrophysics

Quantitative spectroscopy of single and multiple OB-type stars

Non-LTE spectrum analysis with machine learning

P. Aschenbrenner* and N. Przybilla*

Universität Innsbruck, Institut für Astro- und Teilchenphysik, Technikerstr. 25/8, 6020 Innsbruck, Austria

Received 3 January 2026 / Accepted 5 February 2026

ABSTRACT

Aims. The plethora of spectra of OB-type stars in observatory archives and the much larger numbers to come from the WEAVE and 4MOST spectroscopic facilities require efficient, but also accurate and precise methods for (semi)automatic quantitative analyses.
Methods. Neural networks were used to emulate the spectra of single- and multi-star systems, trained on hybrid non-local thermodynamic equilibrium models that cover a wide range of atmospheric parameters and chemical compositions. To derive the full set of stellar atmospheric parameters and uncertainties, a Markov chain Monte Carlo algorithm was implemented to fit high-resolution spectra within 3000–10 500 Å.
Results. The neural networks and fitting algorithm were bundled into a programme called Spectral Analysis Tool Using Restricted Neural networks (SATURN). In its current implementation, SATURN facilitates the emulation of synthetic spectra for spectral types O7 to B9, which differ only negligibly from computed models. SATURN was tested on a number of benchmark stars that have been studied before, including single OB stars and a detached eclipsing binary (DEB) system. Excellent agreement of atmospheric parameters and elemental abundances for up to ten metal species is found with respect to the data in the literature, often with reduced uncertainties of about 1% in effective temperature and 0.05 dex in surface gravity (1σ values). For DEB components, the uncertainties are larger, in particular for the fainter secondaries when only a single-epoch spectrum is considered, and lower if surface gravities and the effective temperature ratio from previous detailed light curve and orbital dynamics studies are used as additional fit constraints. Uncertainties of elemental abundances are typically <0.10 dex. Some first applications of SATURN for analyses of new targets are shown to demonstrate its capabilities, such as fast rotators, including HD 149757 (ζ Oph). Consistent results are also found at reduced spectral resolutions relevant for observations with WEAVE and 4MOST.

Key words. stars: abundances – stars: atmospheres – binaries: spectroscopic – stars: early-type – stars: evolution – stars: fundamental parameters

1. Introduction

Quantitative spectroscopy is the most important tool for the study of stellar atmospheres. It allows atmospheric parameters, such as effective temperature $T_{\rm eff}$ and surface gravity $\log(g)$, and the chemical composition to be derived from an investigation of the detailed line spectrum and the global spectral energy distribution (SED). Since the first thorough application of the then newly developed theoretical framework of excitation and ionisation in thermodynamic equilibrium by Payne-Gaposchkin (1925), which led to the identification of hydrogen as the main chemical constituent of stars, the field has reached a high degree of maturity. Despite the concept of local thermodynamic equilibrium (LTE) for the description of the local state of matter in stellar atmospheres being questioned early (Gerasimovič 1929) – requiring consideration of the so-called non-LTE effects – LTE has remained a foundation for applications until today because of its simplicity and effectiveness in many cases.

However, a pure LTE description has been identified early as insufficient to characterise the atmospheres of hot massive stars of spectral types O and B (OB-type stars) and their progeny because of their intense radiation fields, with further deviations driven by low collision rates in the low-density plasmas of evolved stars. Non-LTE model atmospheres and spectrum synthesis became more realistic over decades due to methodological progress, the development of fast computers, efficient numerical algorithms for solving the radiative transfer and kinematic equilibrium equations, and the provision of the required atomic data, including opacities; for a historic overview of the landmark developments, readers can refer to the first chapter of Hubeny & Mihalas (2015). Currently, several codes exist to compute expanding line-blanketed non-LTE model atmospheres in spherical geometry for OB stars, mainly CMFGEN (Hillier & Miller 1998), FASTWIND (Puls et al. 2005, 2020), POWR (Gräfener et al. 2002; Hamann & Gräfener 2003; Sander et al. 2015), WM-basic (Pauldrach et al. 2001), and METUJE (Krtička & Kubát 2017), which are suited for quantitative analyses throughout the entire OB-star range. They are complemented by the line-blanketed full non-LTE TLUSTY code (Hubeny 1988) and a hybrid non-LTE approach consisting of the ATLAS LTE line-blanketed model atmosphere code (Kurucz 1993, 1996) coupled to the non-LTE line-formation package DETAIL/SURFACE (Giddings 1981; Butler & Giddings 1985, plus further developments), abbreviated as ADS henceforth, as introduced by Przybilla et al. (2006a), Nieva & Przybilla (2007), Weßmayer et al. (2022), and Aschenbrenner et al. (2023). Both TLUSTY and ADS assume hydrostatic equilibrium and plane-parallel geometry; they are therefore applicable to less-luminous OB stars where the line-forming photospheric layers are not significantly affected by the mass outflow. Overall, good consistency between

* Corresponding authors: patrick.aschenbrenner@student.uibk.ac.at; norbert.przybilla@uibk.ac.at

the results obtained with the different codes is found, despite some different assumptions being made, although variances in some details remain, which are often related to choices in atomic data.

The sample size of analysed OB stars has increased greatly over the past three decades, driven by instrumental developments. While initially only single spectra were recorded using slit or fibre-fed spectrographs, several multiplexing approaches have been followed more recently. Multi-slit spectrographs increased the number of simultaneously recorded spectra to around twenty (e.g. Kudritzki et al. 2012, 2014), while fibre-fed multi-object spectroscopy provides data for more than a hundred targets simultaneously, such as those used in the VLT-FLAMES (Very Large Telescope Fibre Large Array Multi Element Spectrograph) survey of massive stars and the VLT-FLAMES Tarantula Survey (Evans et al. 2005, 2011), and independent analyses of these (Urbaneja et al. 2017), or studies of clusters containing massive stars within the Gaia-ESO survey (Blomme et al. 2022; Morel et al. 2022). Integral field spectroscopy promises an even higher multiplex (e.g. Castro et al. 2018), which, however, is restricted by the spatial density of OB stars in reality (e.g. Evans et al. 2019; González-Torà et al. 2022). The limitations of these high-multiplex observations are spectral resolution, wavelength coverage, or both. Important high-resolution quantitative spectroscopy is therefore still based on single-target spectrographs, such as those used within the IACOB project (Simón-Díaz et al. 2020) or the XShootU project (Vink et al. 2023), which considers hundreds of stars. Large spectroscopic surveys of OB stars with new facilities such as the William Herschel Telescope Enhanced Area Velocity Explorer (WEAVE, Jin et al. 2024) and the 4-metre Multi-Object Spectroscopic Telescope (4MOST, de Jong et al. 2019) will even provide spectra for tens of thousands of OB stars. These surveys will comprise a variety of objects, slow to fast rotators, single, binary, and multiple objects (most OB stars turn out to have companions, Chini et al. 2012; Sana et al. 2012), and chemically peculiar stars. Powerful algorithms are required to address the quantitative analysis.

A data-driven approach, such as that implemented for cool star analysis, trained on the known properties of a set of hundreds of observed reference stars (The Cannon, Ness et al. 2015), is difficult to transfer to the analysis of OB stars, as their spectra are sufficiently unique per object; this is in stark contrast to the similarity of the spectra of solar-type stars and red giants. Algorithms that employ classical equivalent width measurements for the analysis of OB star spectra have become rare, with the grid-based deep learning system described by Flores et al. (2023) being an example. Ubiquitous are grid-based χ^2-minimisation routines that compare synthetic to observed spectra, as, for example, discussed in the context of hot star analyses by the Gaia-ESO survey (Blomme et al. 2022; see also Araya et al. 2025). Variants that use on-the-fly model calculations instead of precomputed grids exist, such as the genetic algorithms described by Mokiem et al. (2005) or Tamajo et al. (2011). A different concept is realised in algorithms using principal component analysis (PCA) in combination with a learning database, which, as a main advantage, offers the possibility to drastically reduce dimensionality. One implementation is described by Blomme et al. (2022), another one is the code Maui (Urbaneja et al. 2008; Urbaneja 2026), which, in addition uses a Markov chain Monte Carlo (MCMC) algorithm to constrain uncertainties. Algorithms rarely facilitate the modelling of composite spectra of binaries (e.g. Irrgang et al. 2014). Instead, the usual approach followed relies on spectral disentanglement with subsequent individual spectrum analysis (e.g. Pavlovski et al. 2023), but at the cost of time-series spectroscopy.

Usually, these algorithms extract only a restricted set of parameters, such as a subset of atmospheric and wind parameters, and in addition abundances for a few elements (restricted by the availability of trustworthy model atoms). The full information accessible from the multitude of spectral lines, in particular in high-resolution spectra, is typically not obtained. This also affects the reliability of parameter extraction of spectra of faster rotating stars or lower-resolution spectra, where either the broad rotational profiles or the instrumental broadening (or both) smear out the various individual lines into broad, complex blends. However, including all elements present in stellar atmospheres for the spectrum synthesis comes at the cost of increasing computation time, and, in the worst case, an exponentially growing grid of models is needed for classical interpolation methods. By training a neural network to emulate model spectra, the number of models required can be kept manageable (such as in the PCA approach). Such spectral emulators have already been used to analyse spectra for large-scale surveys of late-type stars using LTE models and full spectrum synthesis (Payne, Ting et al. 2019), with refinements of the approach also being discussed (TransformerPayne, Różański et al. 2025). Extensions of Payne with non-LTE models of late-type stars were done by Kovalev et al. (2019) and applied to binary stars in the Large Sky Area Multi-Object fiber Spectroscopic Telescope Medium Resolution Survey (LAMOST MRS, Liu et al. 2020) by Kovalev et al. (2022). In the context of early-type stars of spectral types A, B, and O over 330 000 objects were analysed in LTE by Xiang et al. (2022, HotPayne) and, independently, by Sun (2025, Slam-Payne). Analyses of high-resolution spectra with LTE models were done with Zeta-Payne (Straumit et al. 2022) for single stars (Gebruers et al. 2022) as well as a binary system (Kovalev & Straumit 2023). Ideally, the analysis of early-type stars requires an extension to non-LTE modelling.

Currently missing is a method to extract basically all available information on stellar parameters and elemental abundances in an efficient but still accurate and precise manner from ground-based spectroscopy of OB stars with charge-coupled device detectors, that is, from the atmospheric cut-off in the near-ultraviolet over the optical to the near-infrared. This shall be applicable to slow and fast rotators alike, to single and multiple stars. In the present work, we discuss an approach that solves this issue in a mostly automated fashion.

The paper is structured as follows. An overview of the calculated models and the emulation method with neural networks is given in Sect. 2. A general method for fitting spectra of single and multi-star systems is introduced in Sect. 3. The results of the analysis of five single benchmark stars and one binary system, as well as additional science targets, and their discussion are summarised in Sect. 4. A general summary and outlook is provided in Sect. 5. In Appendix A we provide details on the neural network training process, Appendix B contains notes on the determination of the microturbulence velocity. The Appendices C and D concentrate on SEDs and exemplary fits to the observed spectra of some of the sample stars. Finally, Appendix E focuses on the applicability of the analysis methodology introduced here to data at lower spectral resolution, such as those to be provided by WEAVE and 4MOST.

2. Model atmospheres and spectrum synthesis

For our model calculations, we subdivided the $T_{\rm eff}$ - $\log(g)$ space covering the OB-type stars that we intend to analyse into five overlapping regions as shown in Fig. 1, labelled O, B_1, B_2, BSG_1, and BSG_2. Each region includes different ionisation

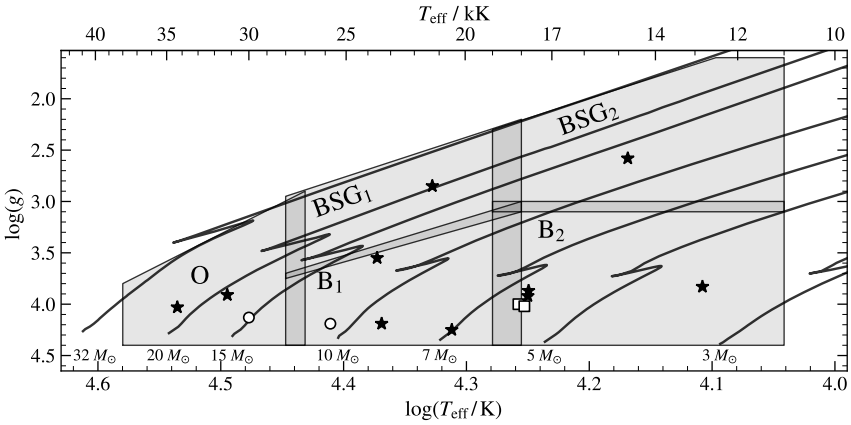

Fig. 1. Kiel diagram showing the five different regions of model coverage (O, B_1, B_2, BSG_1, and BSG_2). Overlayed are Ekström et al. (2012) evolutionary tracks for rotating stars ($v_{\rm ini}/v_{\rm crit} = 0.4$) at solar metallicity (black lines) for different masses, as indicated. The five-pointed black stars mark the positions of the single stars analysed in the present work and the matching open symbols are the components in the analysed binary systems.

Table 1. Model atoms for non-LTE calculations with DETAIL.

Ion	Terms	Transitions	Reference
H I	25	300	[1]
He I/II	29+6/20	162/190	[2]
C I/II/III/IV	80/68/70/53	669/425/373/319	[3]
N I/II/III/IV	89/77/47+3/84+6	668/462/410/1123	[4]
O I/II/III	51/177+2/132+2	243/2560/1515	[5]
Ne I/II	153/78	952/992	[6]
Mg I/II	88/37	471/236	[7]
Al II/III	54+6/46+1	378/272	[8]
Si II/III/IV	52+3/68+4/33+2	357/572/242	[9]
P II/III/IV	45/25/23	358/81/61	[10]
S II/III	78/21	302/34	[11]
Fe II/III/IV	265/60+46/65+70	2887/2446/2094	[12]

Notes. [1] Przybilla & Butler (2004); [2] Przybilla (2005); [3] Przybilla et al. (2001b), Nieva & Przybilla (2006, 2008); [4] Przybilla & Butler (2001), Przybilla & Aschenbrenner (in prep.); [5] Przybilla et al. (2000), Przybilla & Butler (in prep.); [6] Morel & Butler (2008); [7] Przybilla et al. (2001a); [8] Przybilla (in prep.); [9] Przybilla & Butler (in prep.); [10] Aschenbrenner et al. (2025); [11] Vrancken et al. (1996), updated; [12] Becker (1998), Morel et al. (2006).

stages of the elements in the non-LTE calculations that prevail at the given atmospheric parameter ranges, but all models within a region were calculated in a consistent way. The upper $T_{\rm eff}$ boundary is defined by the transition towards the appearance of stronger radiatively driven winds, which, similar to the lower log(g)-value envelope, imply a limit for the assumption of hydrostatic equilibrium for the stellar photospheric layers. The upper log(g) boundary is defined by about the location of the zero-age main sequence (ZAMS), and at the lower $T_{\rm eff}$ boundary lines of chemical species that are not covered by our model atoms start to become relevant, for example Cr II, so that the spectrum synthesis starts to lose completeness.

2.1. Models and programmes

For each region ~5000 model spectra with randomly sampled parameters were calculated. The free parameters of the models are effective temperature $T_{\rm eff}$, surface gravity log(g), microturbulence velocity ξ, helium abundance by number y, and abundances for ten metals (see Table 1). The model parameters were drawn from discrete uniform distributions with step sizes of 50 K for $T_{\rm eff}$, 0.01 dex for log(g), 1 km s^{-1} for ξ, 0.01 for y, and 0.05 dex for the abundances of all other elements. The lower

Table 2. Parameter ranges coverage by the models in different regions.

Region	$T_{\rm eff}$ K	log(g) cgs	ξ km s^{-1}	N log(N/H)+12
O	27 000–38 000	2.90–4.40	0–17	7.00–8.60
B_1	18 000–28 000	3.00–4.40	0–16	7.00–8.60
BSG_1	18 000–28 000	2.20–3.75	0–15	7.40–9.00
B_2	11 000–19 000	3.00–4.40	0–14	7.00–8.60
BSG_2	11 000–19 000	1.60–3.10	0–14	7.40–9.00

and upper limits for the parameters dependent on the region and are listed in Table 2. The helium abundance for all models is in the interval [0.07, 0.15] and the limits of the metal abundances, except nitrogen, are chosen to be ±0.8 dex of the cosmic abundance standard (CAS, Nieva & Przybilla 2012; Przybilla et al. 2013; Aschenbrenner et al. 2025). The choices for the extent of the parameter ranges in ξ, y and for the metal abundances were motivated by typical values that we have found in previous investigations, with some extra security margin, motivated by stellar evolution model predictions (in the case of helium) and the presence of abundance gradients in the Milky Way (metals). Each model was computed with the hybrid non-LTE approach using ADS in an implementation close to that described by Aschenbrenner et al. (2023). We briefly mention a few key ingredients: the use of ATLAS12 models allows the effects of turbulent pressure to be considered on the atmospheric structure; use of an accelerated lambda iteration scheme (Rybicki & Hummer 1991) that allows complex model atoms to be handled; use of an occupation probability formalism (Hummer & Mihalas 1988; Hubeny et al. 1994) for hydrogen to facilitate a better modelling of the series limits; use of up-to-date Stark-broadening tables for hydrogen and helium (Tremblay & Bergeron 2009; Beauchamp et al. 1997; Dimitrijevic & Sahal-Brechot 1990; Schoening & Butler 1989). For the non-LTE calculations we adopted state-of-the-art model atoms, listed in Table 1, which experienced some updates over the years. For each element, the different ions considered are listed with the number of explicit terms (plus superlevels), the number of radiative bound-bound transitions per ion (we note in particular the use of highly accurate and precise oscillator strengths of Froese Fischer & Tachiev 2004; Froese Fischer et al. 2006), and references. The model atoms also consider photoionisation cross-sections and large sets of collisional data from ab initio calculations. All model atoms are completed by the ground energy term of the next-higher ion.

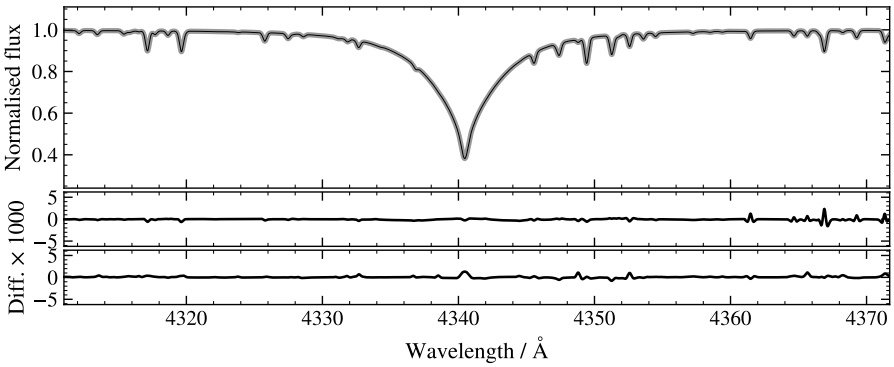

Fig. 2. Comparison between a model spectrum calculated with ADS and the spectra created with the neural networks. Top panel: the normalised spectrum of an ADS model with $T_{\rm eff} = 18\,500$ K and $\log(g) = 3.10$ (grey line) is compared to the spectrum created with the neural network from the B_1 region with the same parameters (black line). Middle panel: difference between the two spectra. Bottom panel: difference between the ADS model spectrum and the spectrum created with the neural network from the B_2 region.

2.2. Single-star models

The normalised flux $f_{\lambda_i}(\Theta)$ at each wavelength point λ_i is a function of the 14 different parameters included in the model calculations, where all parameters are combined into a vector Θ. Based on the universal approximation theorem (Hornik et al. 1989), we used our calculated models to train five neural networks, one for each region, to predict the flux for given input parameters. The neural networks can then be used to generate the models for arbitrary combinations of atmospheric parameters. The models calculated with SURFACE provide the flux values at a few hundred thousand points λ_i. Instead of training a single neural network to predict all spectrum points at once, we split the entire covered wavelength range into smaller chunks, each one covering ∼7500 points and having its own network. The architecture of these smaller neural networks is a multilayer perceptron and we implemented it with PyTorch (Paszke et al. 2019). The input layer has 14 neurons, one for each parameter, there are three hidden layers with 32/64/128 neurons, respectively, using the sigmoid activation function $\sigma(x) = (1 + e^{-x})^{-1}$, and the output layer has ∼7500 neurons. The full spectrum is created by concatenating the outputs of the different neural networks. This approach allows for fitting optimisations since often only small parts of a spectrum are considered for the analysis. For the training, we split the calculated models into a training set and a testing set, the details are summarised in Appendix A.

This procedure was repeated for each of the five parameter regions. For validation, we looked at the overlaps between the regions and compared a model spectrum computed with ADS, which was not used for training, with the spectra predicted by the neural networks. This is shown in Fig. 2 for the regions B_1 and B_2. In general, we found that the absolute difference between model spectra calculated with ADS in the testing set and the model spectra generated with neural networks is below 4.2E−5 for 50% for all the spectrum points and below 2.8E−4 for 99% of all the points. The differences reach a maximum value of about $2.0E{-}3$ in the cores of a few spectral lines.

2.3. Multi-star models

Equation (1) of Aschenbrenner & Przybilla (2024) can be employed to construct the normalised composite spectrum $f_{\rm comp}$ of multi-star systems from the spectra of individual stars

$$f_{\rm comp} = \frac{\sum_i w_i f_{{\rm cont},i} f_i}{\sum_i w_i f_{{\rm cont},i}}, \quad (1)$$

where f_i is the normalised flux of the i-th star and $f_{{\rm cont},i}$ the corresponding continuum flux, and w_i a weight factor that matches the ratio of effective surface area of each star relative to the primary (for non-interacting stars). Again, we trained a neural network for each of the five regions to emulate the continuum flux of the calculated models. However, the neural networks for continuum emulation do not predict the flux at each wavelength point, only at ∼150 pre-defined wavelength points. Then, natural cubic splines are used to interpolate between those points.

3. Spectral analysis

3.1. Observational data

In this work, we use high-resolution spectra with a resolving power of $R = \lambda/\Delta\lambda \approx 40\,000$ to 115 000 and wide wavelength coverage. For two stars, as indicated in Table 3, we used spectra taken with the Fibre Optics Cassegrain Echelle Spectrograph (FOCES, Pfeiffer et al. 1998) on the 2.2 m telescope at the Calar Alto Observatory in Spain; another three objects were observed with the Fiberfed Extended Range Optical Spectrograph (FEROS, Kaufer et al. 1999) on the 2.2 m telescope of the Max-Planck-Gesellschaft and the European Southern Observatory (ESO) at La Silla in Chile. One star was observed with the Fibre-fed Echelle Spectrograph (FIES, Telting et al. 2014) on the 2.5 m Nordic Optical Telescope at La Palma, five stars were observed with the Echelle Spectro-Polarimetric Device for the Observation of Stars (ESPaDOnS, Manset & Donati 2003) on the 3.6 m Canada-France-Hawaii telescope (CFHT) at Mauna Kea in Hawaii, and the spectrum of one object was taken with the High Accuracy Radial velocity Planet Searcher (HARPS, Mayor et al. 2003) at the ESO La Silla 3.6 m telescope. For test purposes, we also employed intermediate-resolution spectra ($R \approx 5000$, 10 000 and 20 000) observed with XSHOOTER (Vernet et al. 2011) on the ESO Very Large Telescope.

The data reduction for the spectra of HD 214680, HD 35299, HD 91316, and HD 164353 is described in previous works, see the references in Table 3; for the processing of the HD 160762 raw data see Irrgang (2014). In the case of HD 259135, HD 149757, HD 87015, and HD 17081 we downloaded pipeline-reduced spectra from the CFHT Science Archive at the Canadian Astronomy Data Centre[1] and for HD 93827, HD 112092, HD 77464, and for the XSHOOTER data of HD 35299 we downloaded Phase 3 data from the ESO Science Portal[2]. The spectra were normalised by fitting a cubic spline function through carefully selected continuum points. The signal-to-noise ratios (S/Ns) measured at ∼5000 Å are also indicated in Table 3.

3.2. Model fitting

To use the neural networks for spectral analysis, we wrote a programme called Spectral Analysis Tool Using Restricted

[1] https://www.cadc-ccda.hia-iha.nrc-cnrc.gc.ca/en/cfht/
[2] https://archive.eso.org/scienceportal/home

Table 3. Properties of the sample stars and their atmospheric parameters.

Object	Sp. Type	Instrument	S/N	$T_{\rm eff}$	$\log(g)$	y	ξ	$v \sin i$	ζ	Ref.
				K	(cgs)	by number		km s^{-1}		
benchmark stars:										
HD 214680 (10 Lac)	O9 V	FOCES	500	34 550±300	4.04±0.05	0.083±0.009	5±2	14±1	32±2	1
				34 305±250	4.03±0.04	0.092±0.010	6.1±0.5	11.3±0.7	34.5±0.4	
HD 35299	B1.5 V	FOCES	350	23 500±300	4.20±0.05	0.089	0±1	8±1	...	2
				23 391±521	4.19±0.06	0.092±0.002	0.5±0.6	1.4±0.8	8.3±0.2	
HD 91316 (ρ Leo)	B1 Iab	ESPaDOnS	750	21 700±200	2.87±0.04	0.092±0.009	15±2	43±5	62±5	3
				21 270±201	2.85±0.02	0.091±0.008	15.2±0.5	42.4±0.5	63.8±0.5	
HD 160762 (ι Her)	B3 IV	FIES	500	17 500±200	3.85±0.05	0.089	1±1	6±1	...	2
				17 759±140	3.87±0.03	0.086±0.003	1.1±0.8	0.8±0.6	8.1±0.2	
HD 164353 (67 Oph)	B5 Ib	FEROS	500	14 700±300	2.57±0.05	0.091±0.004	8±2	20±4	32±5	4
				14 745±116	2.58±0.02	0.094±0.007	8.3±1.4	16.0±1.0	33.8±0.8	
HD 259135 (V578 Mon)	DEB	ESPaDOnS	550							
HD 259135 A	B1 V			30 000±500	4.13±0.02	...	4±1	117±4	...	5, 6
				30 117±457	4.12±0.07					
				29 829±243	4.13±0.02	0.094±0.009	2.5±0.2	114.8±0.6	16.7±3.9	
HD 259135 B	B2 V			25 750±435	4.19±0.02	...	2±1	94±2	...	
				25 046±988	4.21±0.15					
				25 587±213	4.19±0.02	0.090±0.009	1.1±0.8	89.6±2.5	57.4±5.8	
new applications:										
HD 149757 (ζ Oph)	O9.2 IVnn	ESPaDOnS	800	31 238±753	3.72±0.10 [a]	0.131±0.011	7.7±3.4	382±4	...	
HD 93827	B2 Ib/II	FEROS	220	23 590±950	3.44±0.09 [b]	0.101±0.009	14.2±3.5	241±1	14±7	
HD 112092 (μ^1 Cru)	B2 IV	FEROS	500	20 508±245	4.25±0.05	0.090±0.006	1.8±1.2	31.3±0.2	13.3±0.6	
HD 87015 (EO Leo)	B2 V	ESPaDOnS	480	17 782±365	3.92±0.05	0.101±0.008	2.7±1.1	214±1	45±4	
HD 17081 (π Cet)	B8 IV	ESPaDOnS	600	12 800±200	3.75±0.10	0.107±0.010	1.0±0.5	20.2±0.9	...	7
				12 819±76	3.83±0.03	0.124±0.005	1.6±0.1	19.9±0.1	0.4±0.3	
HD 77464 (CV Vel)	DEB	HARPS	250							
HD 77464 A	B2.5 V			18 100±500	4.00±0.01	...	...	21.5±2.0	...	8
				18 085±455	4.00±0.17					
				18 064±244	4.00±0.01	0.094±0.005	1.4±1.0	11.4±0.4	11.3±0.5	
HD 77464 B	B2.5 V			17 900±500	4.02±0.01	...	...	21.1±2.0	...	
				17 758±486	4.01±0.16					
				17 647±269	4.02±0.01	0.102±0.004	2.2±1.6	2.5±1.2	27.7±0.3	

Notes. For the benchmark stars the first row lists the literature values, the second row the values derived in this work. For the detached eclipsing binaries three solutions are given: previous literature results in the first row, the second row provides values derived from the single epoch spectrum adopted here alone, the third row gives our results using the $\log(g)$ values and the $T_{\rm eff}$ ratio (if known) from the binary solution based on the light curve and radial-velocity analysis as additional fit constraints. Uncertainties are 1σ values. [a] $\log(g_{\rm true}) = 3.91 \pm 0.07$, see Sect. 4.3; [b] $\log(g_{\rm true}) = 3.55 \pm 0.07$. (1) Aschenbrenner et al. (2023); (2) Nieva & Przybilla (2012); (3) Weßmayer et al. (2023); (4) Weßmayer et al. (2022); (5) Garcia et al. (2014); (6) Pavlovski et al. (2018); (7) Fossati et al. (2009); (8) Albrecht et al. (2014).

Neural networks (SATURN). For comparisons between models generated with the neural networks and the observed spectra, the model spectra are broadened with rotational and radial-tangential macroturbulence profiles (Gray 2005), assuming a linear limb darkening law, and a Gaussian instrumental profile, which depends on the resolving power of the instrument used for observation. SATURN was implemented in Python (with some sub-routines written in C) and provides a graphical user interface which allows to interactively change model parameters and to see the effects on the spectrum in real time. Multi-star systems with any number of stars are supported by implementing composite spectra according to Eq. (1).

The time it takes to generate a model spectrum of a single star using the neural networks and to apply the broadening to it is 10 ms on a fast contemporary central processing unit (vs. ~2 h for the single model computation using ADS). With the ability to create model spectra in such a short time, we use a MCMC fitting algorithm to derive the stellar parameters. We implemented a random-walk Metropolis algorithm (Metropolis et al. 1953), where the fit-parameters are sampled from uniform distributions. The new parameters are accepted with a probability of $\min(1, L(\Theta_i)/L(\Theta_{i-1}))$, where $L(\Theta_i)$ is the likelihood of the model with new parameters and $L(\Theta_{i-1})$ the likelihood of the model with the previous parameters. We define the likelihood function as

$$L(\Theta) \propto \exp\left(\sum_p \frac{1}{n_p} \sum_{\lambda_i} - \frac{\left(f_{\lambda_i,\rm obs} - f(\Theta)_{\lambda_i,\rm mod}\right)^2}{2 \cdot \left(\sigma^2_{\lambda_i,\rm stat} + \sigma^2_{\lambda_i,\rm sys}\right)} \right), \quad (2)$$

where $f_{\lambda_i,\rm obs}$ is the observed flux at point λ_i, $f(\Theta)_{\lambda_i,\rm mod}$ is the model flux at the same wavelength, $\sigma_{\lambda_i,\rm stat}$ the statistical uncertainty of the observed flux and $\sigma_{\lambda_i,\rm sys}$ the systematic uncertainty of the model. We sum over different spectral windows p, covering n_p wavelength points each. The factors $1/n_p$ correspond to taking the mean log-likelihood of each spectral window, weighting each window the same. Otherwise, weak metal lines would have almost no significance compared to the much broader hydrogen and helium lines. The statistical uncertainty depends

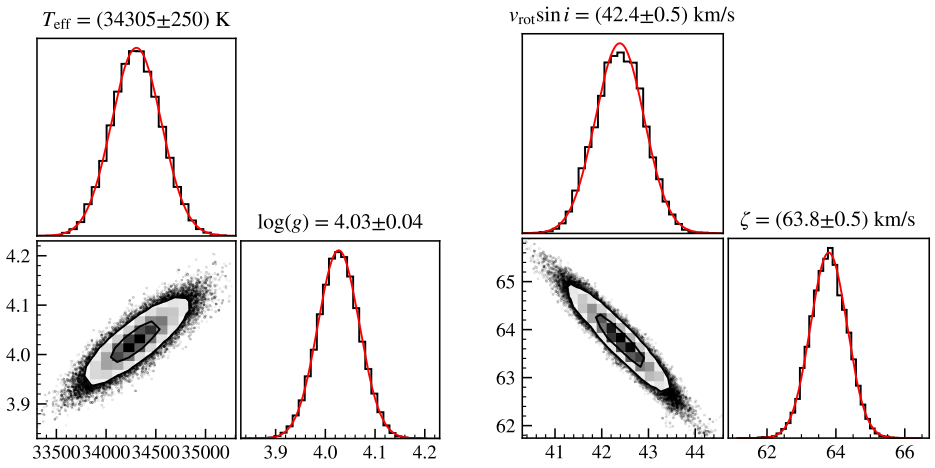

Fig. 3. Exemplary corner plots of the MCMC fit results. In each example the bottom left shows the 2D histogram with 1σ and 2σ contours. The two adjacent plots show 1D histograms for the parameters (black) and a Gaussian (red) with same mean and standard deviation. Left panel set: $T_{\rm eff}$ and log(g) determination for the benchmark test star HD 214680. Right panel set: $v \sin i$ and ζ determination for HD 91316.

on the S/N of the observation $\sigma_{\lambda_i,\rm stat} \approx \sqrt{f_{\lambda_i,\rm obs}}/(\rm S/N)$ and we assume a constant systematic uncertainty of $\sigma_{\lambda_i,\rm sys} = 0.001$ for our model spectra.

With SATURN any combination of atmospheric parameters, projected rotational velocity $v \sin i$ and macroturbulence velocity ζ can be fitted simultaneously. In the case of multi-star systems, the weights and the Doppler shift of the individual stars can be selected as additional fit-parameters. Although it is possible to fit all parameters simultaneously, in the present work we follow a more systematic process of iteratively deriving individual parameters, as described in the following.

3.3. Atmospheric parameter and abundance determination

Effective temperature and surface gravity. To determine $T_{\rm eff}$ and log(g), we simultaneously fit the gravity sensitive wings of hydrogen Balmer lines together with the spectral lines of different ions for the same element to achieve ionisation equilibrium. The fit-parameters are $T_{\rm eff}$, log(g), and the chemical abundances of all elements used for ionisation equilibrium evaluation. An example of a corner plot of the MCMC fit result for the correlated $T_{\rm eff}$ and log(g) determination in HD 214680 is shown in Fig. 3. We note the very tight uncertainty distributions.

Projected rotational velocity and macroturbulence. Both parameters are derived simultaneously by fitting the line profiles of numerous metal lines. The fit-parameters are $v \sin i$, ζ, and the abundances of the elements involved. We use a slight deviation of Eq. (2), adopting $n_p = 1$, corresponding to a classical maximum likelihood fit. A corner plot of the MCMC fit result of the anti-correlated $v \sin i$ and ζ determination in HD 91316 is also shown in Fig. 3, again with very tight uncertainty distributions.

Microturbulence. Usually, the microturbulent velocity ξ is adjusted such that the element abundance of the individual lines becomes independent of the line strength (measured via the equivalent width). Instead, ξ can be adjusted so that the variance of all individual line abundances is minimised, which is equivalent as we show in Appendix B. This approach can also be used to determine ξ in fast-rotating stars and multi-star systems, where the equivalent widths cannot be determined due to blended lines. To determine the microturbulence in this work, we fitted multiple spectral lines of a single element using Eq. (2), which yields the right value for ξ based on some assumptions, as we also show in Appendix B.

Elemental abundances. With all other parameters fixed, the abundances of elements are determined by fitting each individual spectral line of an element and then taking the mean and standard deviation as the atmospheric abundance and uncertainty.

Multi-star systems. Analysing spectra of multi-star systems includes an initial step to determine the radial velocity shift of the individual components. Otherwise, the procedure is exactly the same as described above, only the number of fit-parameters increases at each step to account for all stars in the system.

3.4. Limitations

Although we cover a wide range of stellar parameters of OB stars with the present implementation of SATURN, there are still limitations to the analysis method within the covered area in Fig. 1. A large object class not suitable for analysis is the chemically peculiar stars. In our B_1 region lie the magnetic He-strong stars, which show helium number fractions of typically 0.2–0.3 (e.g. Zboril et al. 1997), while a few more extreme examples exist, with $y = 0.60$ or even 0.95 (González et al. 2019; Przybilla et al. 2021), which lead to markedly different atmospheric structures not covered here. At cooler temperatures towards and within the B_2 region, the He-weak, HgMn, and Bp stars (e.g. Smith 1996) are present. At lower rotational velocities ($v_{\rm rot} < 120\,{\rm km\,s^{-1}}$) atomic diffusion (Michaud 1970) occurs in the then very stable atmospheres and leads to abundances outside the covered intervals, and in particular to very high abundances of otherwise unobserved (heavy) chemical species at optical wavelengths. Diffusion may even lead to accumulation of the ^{3}He isotope, resulting in unusual profiles for some of the helium lines (e.g. Maza et al. 2014), which we do not consider here due to its rarity of occurrence. On the other hand, the OBN and OBC stars (Walborn 1976) within the parameter boundaries that are a consequence of mixing with nuclear-processed material should be covered by the emulated spectra. There may be very few exceptions, such as the enveloped-stripped B-type subgiant HD 40494 (γ Col, Irrgang et al. 2022), which has extreme abundances of carbon and nitrogen beyond the values considered here. Other rare objects, such as runaway stars from a supernova (SN) explosion in a tight binary system that were polluted by SN debris (e.g. HIP 60350, Irrgang et al. 2010), can be analysed.

A second wide object class that is beyond the capabilities of analysis with SATURN is that of fast-rotating classical Be stars (e.g. Rivinius et al. 2013). The second light introduced by the Keplerian decretion disc surrounding the star also requires to

Table 4. Metal abundances $\varepsilon(X) = \log(X/\mathrm{H}) + 12$ (by number) of the sample stars.

Object	C	N	O	Ne	Mg	Al	Si	P[a]	S	Fe
benchmark stars:										
HD 214680	8.36±0.07	8.11±0.11	8.77±0.06	8.24±0.07	7.59±0.03	6.50±0.03	7.48±0.10	5.25	...	...
	8.37±0.08	8.15±0.08	8.71±0.09	8.22±0.08	7.62±0.03	6.52±0.04	7.46±0.10	5.25	...	...
HD 35299	8.35±0.09	7.82±0.08	8.84±0.09	8.07±0.10	7.53±0.06	...	7.56±0.05	5.18±0.06	...	7.53±0.10
	8.35±0.12	7.81±0.07	8.85±0.09	8.10±0.07	7.52±0.05	6.28±0.04	7.52±0.08	5.19±0.04	7.17±0.08	7.49±0.10
HD 91316	7.94±0.08	8.35±0.08	8.44±0.08	8.06±0.06	7.50±0.29	6.27±0.03	7.60±0.09	...	7.20±0.05	7.27±0.09
	8.02±0.10	8.42±0.10	8.44±0.08	8.04±0.07	7.53±0.23	6.30±0.02	7.60±0.13	5.11±0.07	7.19±0.09	7.26±0.09
HD 160762	8.40±0.07	7.89±0.12	8.80±0.09	8.05±0.07	7.56±0.06	...	7.51±0.05	5.40±0.13	...	7.51±0.08
	8.52±0.04	7.85±0.06	8.81±0.04	8.12±0.04	7.53±0.02	6.32±0.07	7.53±0.03	5.42±0.13	7.22±0.11	7.52±0.08
HD 164353	8.31±0.04	8.37±0.06	8.81±0.06	8.05±0.06	7.51±0.05	6.32±0.04	7.65±0.10	5.33±0.06	7.11±0.11	7.63±0.11
	8.29±0.04	8.30±0.05	8.77±0.06	7.99±0.04	7.53±0.07	6.33±0.05	7.61±0.07	5.30±0.05	7.12±0.09	7.68 ±0.11
HD 259135 A	8.18±0.07	7.69±0.12	8.74±0.10	...	7.52±0.10	...	7.50±0.06	...	...	...
	8.26±0.11	7.65±0.14	8.68±0.09	8.13±0.06	7.42	...	7.46±0.05	...	...	...
HD 259135 B	8.21±0.11	7.72±0.09	8.76±0.11	...	7.50±0.10	...	7.44±0.06	...	...	...
	8.38±0.08	7.82±0.14	8.79±0.10	...	7.60	...	7.48±0.05	...	7.16	7.58
new applications:										
HD 149757	8.21±0.09	8.31±0.06	8.72±0.08	8.09	7.72	...	7.76±0.08	...	...	...
HD 93827	8.20±0.10	8.25±0.09	8.62±0.09	...	7.52	6.33±0.02	7.63±0.08	...	7.18	7.51±0.14
HD 112092	8.37±0.04	7.83±0.07	8.78±0.08	8.10±0.07	7.55±0.02	6.31±0.05	7.48±0.05	5.41±0.06	7.29±0.09	7.52±0.12
HD 87015	8.49±0.10	8.07±0.13	8.77±0.08	7.98±0.09	7.40±0.06	6.49±0.05	7.60±0.07	...	7.14±0.08	7.51±0.14
HD 17081	8.48±0.04	8.07±0.07	8.69±0.06	8.10±0.05	7.53±0.04	6.31±0.01	7.67±0.10	5.70±0.03	7.31±0.08	7.70±0.08
HD 77464 A	8.43±0.05	8.12±0.05	8.86±0.06	8.08±0.04	7.54±0.04	6.35±0.06	7.61±0.05	...	7.17±0.07	7.54±0.07
HD 77464 B	8.44±0.03	8.20±0.07	8.86±0.08	8.05±0.06	7.52±0.07	6.38±0.08	7.56±0.09	...	7.16±0.08	7.55±0.08
CAS[b,c,d]	8.35±0.04	7.79±0.04	8.76±0.05	8.09±0.05	7.56±0.05	6.30±0.07	7.50±0.06	5.36±0.14	7.14±0.06	7.52±0.03

Notes. For the benchmark stars the first row lists the literature values (references in Table 3), the second row the values derived in this work. Uncertainties are 1σ values from the line-to-line scatter. If only one line was fitted, no uncertainty is provided. [(a)]Phosphorus literature abundance from Aschenbrenner et al. (2025), [(b)]Nieva & Przybilla (2012), [(c)]Przybilla et al. (2013), [(d)]Aschenbrenner et al. (2025).

be modelled appropriately (e.g. Sigut et al. 2009). Limitations may also occur for stars without discs that rotate fast enough to lead to significant deviations from spherical geometry and gravity darkening. According to the study of Frémat et al. (2005), these effects should be insignificant for angular velocity values relative to the critical one $\Omega/\Omega_c < 0.6$, and then gradually become more and more significant. We remind the reader that critical rotational velocities are about 700, 600, and 500 km s^{-1} for 20, 10, and 5 $M_\odot$ stars on the ZAMS and about 430, 400, and 350 km s^{-1} on the terminal-age main sequence (TAMS).

In multiple-star systems, the composite spectrum can be well modelled as long as the stars are not interacting. Weak binary interactions such as small tidal deformations or small mutual irradiation effects can be accounted for by adjusting the w_i factors in Eq. (1), but in the case of, for example, (over)contact systems, our model spectra computed for single stars are no longer valid.

4. Results

To test and validate the usage of our trained neural networks for future analysis of stellar spectra, we analysed five apparently slowly rotating OB-type stars previously studied on the basis of ADS models in the literature[3], as well as the spectrum of a detached eclipsing binary (DEB) system. The targets cover all five modelling regions shown in Fig. 1. In addition, new applications showcase the capabilities of SATURN.

The results for the stars analysed are summarised in Tables 3 and 4. The former lists the stellar parameters; the name of the object, spectral type, instrument used for observation, signal-to-noise ratio of the spectrum, effective temperature, surface gravity, helium abundance by number, microturbulence velocity, projected rotational velocity, macroturbulence velocity, and a reference for literature values. The latter table lists derived element abundances for up to ten metals.

Overall, we find excellent agreement with the values in the literature for atmospheric parameters as well as element abundances. The small deviations can result from the improved atomic data used for our model calculations or from the usage of different spectra for the analysis. In the following, we provide additional notes for each object analysed, sorted in decreasing order of $T_{\rm eff}$.

4.1. Benchmark star test sample

HD 214680 (10 Lac). This late O-type standard star is constant in radial velocity, and a ∼10 mag (in the I band) fainter star at ∼3.″6 distance (Turner et al. 2008) is irrelevant for spectroscopy. Therefore, 10 Lac can be viewed as a single star; for a

[3] Each of the benchmark stars has been analysed multiple times before. While there is usually general agreement of results obtained with modern codes (see, e.g. Weßmayer et al. 2022; Aschenbrenner et al. 2023), there exist many differences in assumptions, methods and data used for the calculations, such that we refrain from detailed comparisons with all available results in the literature.

detailed discussion of the star, see Aschenbrenner et al. (2023). The derived atmospheric parameters and element abundances for the Morgan-Keenan standard star 10 Lac are in excellent agreement with the literature values. As an indicator for $T_{\rm eff}$, we used the simultaneous ionisation equilibria of He I/II, O II/III, and Si III/IV. The noticeable higher helium abundance derived in this work can be explained by using a different version of DETAIL to calculate the helium occupation numbers. Aschenbrenner et al. (2023) used opacity averaging with opacity distribution functions to avoid the He I singlet problem (Najarro et al. 2006), which results from an overlap of the He I 584 Å resonance line with two Fe IV transitions. In order to keep all of the model calculations consistent and to employ opacity sampling for all calculations, we use the workaround by Puls et al. (2020) and set the oscillator strengths of the involved Fe IV transitions to $\log(gf) = -5$.

HD 35299. To the best of our knowledge, HD 35299 is a single star with constant radial velocity (Morrell & Levato 1991; Chini et al. 2012). It was identified to show both β Cephei and slowly pulsating B-star (SPB) variability by Balona & Ozuyar (2020). As $T_{\rm eff}$ indicator we used the simultaneous ionisation equilibria of O I/II, Ne I/II, and Si III/IV. For this star among our benchmark objects, intermediate-resolution spectra were also available. Tests of SATURN at resolutions relevant for upcoming observations with WEAVE and 4MOST were therefore feasible. Consistent results on the stellar parameters are also obtained in that case; see Appendix E for details.

HD 91316 (ρ Leo). The star is a rare supergiant at high galactic latitude, which has reached its position as a runaway star from the galactic disc. Occultations by the moon have indicated a binary nature, with the companion resolved later by speckle interferometry, being located at a distance of 46.1 mas, and showing a magnitude difference in V of 1.5 mag (Tokovinin et al. 2010); for a more detailed discussion of the star, see Weßmayer et al. (2023). In order to compare with the literature values, we treated the spectrum as that of a supposedly single star. For the analysis, we used the ionisation equilibria of N II/III, O I/II, Ne I/II, and Si III/IV. We obtained a slightly lower effective temperature compared to the previous literature value, however, all the derived parameters are still compatible.

HD 160762 (ι Her). The β Cep pulsator ι Her is a single-lined spectroscopic binary star (SB1), with a secondary of unknown spectral type in an eccentric ($e = 0.54\pm0.03$) 111.5±0.1 d orbit (Bätz et al. 2026). The companion does not contribute to the spectrum and – because ι Her does not show a CNO mixing signature – is likely of significantly later spectral type than the primary, and not a white dwarf (which in view of the small minimum semi-major axis of $12.68\pm0.74\,R_\odot$ would otherwise imply a previous mass exchange). For deriving $T_{\rm eff}$, we used simultaneously the ionisation equilibria of O I/II, Al II/III, Si II/III, and Fe II/III. All the derived parameters and abundances agree excellently with the literature values except for the carbon abundance, where we derive a ∼0.1 dex higher value. The model atom for C II saw some extension with regard to the inclusion of additional energy levels in the quartet spin system, enabling the use of additional spectral lines for analysis but also leading to slightly different level populations overall. We also use a higher-quality spectrum for the analysis; both together likely result in the small shift in abundance.

HD 164353 (67 Oph). This supergiant is a visual multiple star, with the closest companion being about 7″ away and about 10 mag fainter (Mason et al. 2001). Therefore, it is effectively single for the spectroscopic analysis. We used ionisation equilibria of O I/II, Al II/III, and Fe II/III for the determination of $T_{\rm eff}$.

HD 259135 (V578 Mon). This double-lined eclipsing binary is located in the open cluster NGC 2244, near the centre of the Rosette Nebula. The spectrum used for analysis was observed after the secondary eclipse, where the stars have a radial velocity separation of ∼200 km s^{-1}. We provide two solutions for each of the individual stars, using ionisation equilibria of He I/II and Si III/IV for the primary and O I/II for the secondary to determine $T_{\rm eff}$. The first solution is derived on the basis of a single epoch spectrum and we reproduce the same atmospheric parameters as previous works. The much higher uncertainties for the parameters of the secondary star are a consequence of its smaller contribution to the total flux. For the second solution, we use the known surface gravities and the effective temperature ratio of $T_2/T_1 = 0.858\pm0.002$ (Garcia et al. 2014) as fit constraints, to derive the effective temperatures with lower uncertainties. We adopted a weight factor $w = 0.54\pm0.04$ for the analysis (Eq. (1)). This is less than the expected value from pure geometric considerations based on the relative surface areas implied by the stellar radii ($w_{\rm geo} = 0.629\pm0.017$). However, deviations are expected due to mutual irradiation effects in this close binary system. The resulting model fit to the observed spectrum is shown in Appendix D, Fig. D.1.

As a further test, we also calculated the spectroscopic distance $d_{\rm spec} = 1468\pm83$ pc to V758 Mon using Eq. (4) of Aschenbrenner & Przybilla (2024). We corrected the measured apparent magnitude of $m_V = 8.541\pm0.007$ (Mermilliod 1997) for interstellar extinction by a value of $A_V \approx 1.4$ mag, found by fitting the SED, see Appendix C. For the radii, we adopted $R_1 = 5.41\pm0.04\,R_\odot$ and $R_2 = 4.29\pm0.05\,R_\odot$ (Pavlovski et al. 2018). The spectroscopic distance is in excellent agreement with the cluster distance $d_{\rm NGC\,2244} = 1464^{+94}_{-84}$ pc as derived by Aschenbrenner et al. (2023) from considering *Gaia* Early Data Release 3 (EDR3, Gaia Collaboration 2016, 2021) parallaxes for its massive star content. For comparison, the *Gaia* parallax based photogeometric distance to V578 Mon is $d = 1509^{+102}_{-103}$ pc (Bailer-Jones et al. 2021) – which is also in good agreement – with a renormalised unit weight error (RUWE) of 1.3, hinting at the observed binarity.

4.2. Applications

HD 149757 (ζ Oph). This runaway star is the closest O-type star and shows a prominent bow-shock in the IR. It is a very fast-rotating single (Hutter et al. 2021) star with broad spectral lines that show strong variability due to pulsations (e.g. Walker et al. 2005; Kalita et al. 2025). Since the line broadening is dominated by the rotation of the star, we set $\zeta = 0$ km s^{-1} for the analysis. In contrast to the other stars in the analysed sample, we determined $v \sin i$ by fitting multiple He I lines and taking the mean and standard deviation of the individual best fitting velocities. To fit the atmospheric parameters, we used the ionisation equilibria of He I/II and O II/III as temperature indicators and the wings of the Balmer lines to determine surface gravity. We note that the derived $\log(g)$ value in Table 3 is not corrected for centrifugal acceleration, the 'true' (polar) value is significantly larger at such a high rotation rate (see the footnote in Table 3). We want to state the atmospheric parameters determined recently by de Burgos et al. (2024), $T_{\rm eff} = 30\,700\pm600$ K, $\log(g) = 3.30\pm0.09$, $y = 0.130\pm0.030$, and $v \sin i = 410$ km s^{-1}, which show reasonable

agreement with our values; there are many additional studies available in the literature (see e.g. Gordon et al. 2018, their Table 2). The star shows a CNO-mixing signature and enhanced helium, as expected for a fast rotator, but see Sect. 4.3. The strong blending effects due to high rotation preclude the determination of the abundances of several elements, but magnesium and silicon are higher than CAS values. Certainly, the star shows pronounced deformation from spherical geometry and gravity darkening over its surface, such that our approach of an 'average' atmosphere can be expected to introduce an additional systematic error, see the discussion in Sect. 3.4. However, compared to typical uncertainties of abundances in massive stars to the extent of ∼0.3 dex as discussed in the literature, these are still reasonable results if one assumes that they should be close to CAS values like for all OB stars in the solar neighbourhood investigated by us. The model fit to the observed spectrum is shown in Fig. D.2.

HD 93827. This star of luminosity class between bright giant and supergiant is apparently single, located in the Carina spiral feature; it is the faintest and most distant of the stars investigated here. It has been studied in some aspects by Fraser et al. (2010), they adopted $T_{\rm eff} = 18\,500$ K from a spectral type calibration and $\log(g) = 2.70$ from fitting Hγ and Hδ, and the very high $v \sin i$ for such an evolved object attracted our interest. We performed here the first comprehensive analysis of the stellar properties. We confirm the high rotational velocity, but its position in the Kiel diagram (Fig. 1) locates it close to the TAMS, putting it near the end of core hydrogen burning, still not being subject to the rapid envelope extension (and spin-down) thereafter. The star also shows mixing of the surface layers with CNO-cycled material from the core, as expected at fast rotation, but otherwise abundances of the heavier elements are close to CAS values. The model fit to the observation is shown in Fig. D.3.

HD 112092 (μ^1 Cru). This subgiant was recently identified to show SPB pulsations (Balona & Ozuyar 2020), explaining the presence of some bumps in the observed spectral lines. It is constant in radial velocity (Chini et al. 2012), apparently single, and its visual companion μ^2 Cru is too distant to affect spectroscopy. We provide the first non-LTE analysis of this star since Kilian (1994). All abundances are compatible with the CAS values, with sulphur showing a tendency to higher values.

HD 87015 (EO Leo). The star is a fast rotator and apparently a single one. We present here the first comprehensive quantitative spectroscopic investigation; before, atmospheric parameters were determined by Lyubimkov et al. (2002, $T_{\rm eff} = 17\,900\pm300$ K, $\log(g) = 3.86\pm0.09$) and Huang et al. (2010, $T_{\rm eff} = 16\,435\pm150$ K, $\log(g) = 3.694\pm0.020$), which are in agreement with our values in case of the former, and in disagreement in the case of the latter work (where both $T_{\rm eff}$ and $\log(g)$ were derived from fitting only one spectral line, Hγ). Abundances roughly align with CAS values, the nitrogen abundance is elevated as expected for a fast rotator, but at high carbon abundance. Magnesium is slightly underabundant, and aluminium is slightly overabundant, which may be a selection effect due to the inaccessibility of some lines at high rotational velocity. In general, the star is nearly a clone of ι Her, but at high $v \sin i$. A visual inspection of light curves observed with the Transiting Exoplanet Survey Satellite implies β Cep pulsations, another property shared with ι Her.

HD 17081 (π Cet). This is an SB1 star with a nearly circular orbit and a period of 7.45 yr, the secondary probably being a white dwarf (Lacy et al. 1997); for analysis purposes, it can be treated as single. It has been intensely studied in LTE (e.g. Adelman et al. 2002; Fossati et al. 2009) because it is a rare case of an apparently slowly rotating late B-type star that is not notably chemically peculiar. It has also been subject to a hybrid non-LTE abundance analysis (Mashonkina et al. 2020), based on the atmospheric parameters of Fossati et al. (2009). As Mashonkina et al. (2020) used a different model atmosphere code, a different variant of the DETAIL code, their own model atom implementations, and a different line-formation code with their own selection of line-formation parameters, we do not adopt this solution as a benchmark case. However, we note that their abundances (O, Ne, Na, Mg, Ca, Ti, Sr, and preliminary values of Fe) are close to the solar ones, with slightly enhanced carbon and silicon. For the latter two, we find the same and also enhanced abundances of N, P, S, and Fe, whereas the other elements are compatible with the CAS values. Our abundances, together with the enhanced helium, imply the possible occurrence of some mass transfer during the past asymptotic giant branch phase of the companion, and a small amount of atomic diffusion having taken place in π Ceti's atmosphere since then. Finally, we want to note that the $T_{\rm eff}$ and $\log(g)$ determination shows some degeneracy with respect to the helium abundance, with some ionisation equilibria pointing towards a ∼300 K higher effective temperature that would lead to a very similar quality of the overall spectral fit. Reassuringly, the present solution reproduces several photospheric non-LTE emission lines, such as the C I 8335 and 9406 Å singlet lines.

HD 77464 (CV Vel). This DEB system hosts two very similar B-type stars. Both are slowly rotating and show strong metal lines, separated by $\sim$135 km s^{-1} in the spectrum used (see Fig. D.4). Only the broad hydrogen and helium lines overlap and must be fitted simultaneously. From our best global fit we obtained a weight of $w = 1.00\pm0.05$, compatible with the ratio of surface areas calculated from the radii determined by Albrecht et al. (2014), $w = 0.93\pm0.02$. Similar to the case of V578 Mon, the solution based on the single-epoch spectrum alone leads to increased uncertainties, in particular for $\log(g)$, while the additional constraints from the earlier radial velocity and light curve solution (Albrecht et al. 2014) result in very tight uncertainties. We note that our consideration of both, rotational and macroturbulent velocities, for the line broadening leads to significantly different $v \sin i$ values than those of Albrecht et al. (2014). Another factor in this context may also be precession of the rotational axes due to their misalignment as reported by the same authors. The chemical composition of both stars is identical and agrees with CAS values for most elements. However, we find slight elevated abundances of carbon and oxygen, while nitrogen is enriched by >0.3 dex in both stars. A previous abundance analysis of the system's components by Yakut et al. (2007, assuming $T_{\rm eff} = 18\,000$ K for both) yielded overall systematically lower abundances, though still compatible with our values within their typical uncertainties of 0.2–0.6 dex.

We also characterised the extinction towards HD 77464, by fitting the SED using the reddening law of Fitzpatrick (1999), where we set the ratio of total-to-selective extinction, $R_V = A_V/E(B-V) = 3.1$ and obtained a colour excess of $E(B-V) = 0.034\pm0.010$ from a least-square fit. The fitted SED is shown in Fig. C.1. After correcting the measured magnitude of $m_V = 6.706\pm0.008$ (Mermilliod 1997) for extinction and by adopting the radii $R_1 = 4.08\pm0.03\,R_\odot$ and $R_2 = 3.94\pm0.03\,R_\odot$ (Albrecht et al. 2014), we calculated $d_{\rm spec} = 598\pm9$ pc to the system. The *Gaia* photogeometric distance is $d = 565^{+10}_{-13}$ pc (Bailer-Jones et al. 2021), with a RUWE of 0.84.

Table 5. Fundamental stellar parameters.

Object	V^a	$E(B-V)$ (mag)	R_V	$B.C.$ (mag)	$M/M_\odot$	$R/R_\odot$	$\log L/L_\odot$	$\log \tau_{\rm evol}$ (yr)	$d_{\rm spec}$ (pc)	d_{Gaia} (pc)^b
HD 149757	2.567±0.005	0.33±0.02	3.0±0.1	−2.91±0.06	18.7±0.7	7.6±0.6	4.69±0.08	$>6.80^{+0.04}_{-0.04}$	135^{+11}_{-11}	135^{+12}_{-9}
HD 93827	9.320±0.010	0.32±0.02	3.1±0.1	−2.24±0.10	12.9±0.8	11.2±0.8	4.54±0.09	$7.20^{+0.06}_{-0.05}$	3461^{+266}_{-264}	3484^{+231}_{-194}
HD 112092	4.032±0.014	0.04±0.01	3.1±0.1	−2.00±0.03	7.0±0.1	3.3±0.2	3.24±0.04	$6.98^{+0.20}_{-0.35}$	113^{+7}_{-6}	124^{+5}_{-3}
HD 87015	5.655±0.041	0.01±0.01	3.1±0.1	−1.62±0.05	6.3±0.2	4.6±0.3	3.28±0.05	$7.68^{+0.03}_{-0.04}$	310^{+20}_{-20}	308^{+8}_{-8}
HD 17081	4.241±0.006	0.00±0.01	3.1±0.1	−0.80±0.03	4.0±0.1	4.0±0.2	2.60±0.03	$8.19^{+0.01}_{-0.01}$	109^{+5}_{-4}	119^{+2}_{-3}

Notes. Uncertainties are 1σ values. [(a)]Mermilliod (1997), [(b)]Bailer-Jones et al. (2021).

As a test of our derived parameters, we made sure that the position of our sample objects in the Kiel diagram ($\log(g)$ vs. $\log T_{\rm eff}$), the Hertzsprung-Russell diagram (HRD, $\log L/L_\odot$ vs. $\log T_{\rm eff}$) and the spectroscopic HRD (sHRD, $\log(\mathscr{L}/\mathscr{L}_\odot)$ vs. $\log T_{\rm eff}$, introduced by Langer & Kudritzki 2014, with $\mathscr{L} = T_{\rm eff}^4/g$) is similar relative to evolutionary tracks in all three diagrams. Finally, we also verified that the positions of the stars in the N/C versus N/O diagram (Przybilla et al. 2010; Maeder et al. 2014) are within the expected path for CNO mixing.

4.3. Fundamental stellar parameters

In order to complete the analysis of the new targets, their fundamental stellar parameters are summarised in Table 5. The entries are the Johnson V magnitude, the colour excess $E(B-V)$, the ratio of total-to-selective extinction R_V, bolometric correction $B.C.$, mass M, radius R, luminosity L, evolutionary age $\tau_{\rm evol}$, spectroscopic distance $d_{\rm spec}$, and Gaia EDR3 distance d_{Gaia}. We determined $E(B-V)$ and R_V by fitting the SEDs of the individual objects, see Appendix C for details. In the case of HD 112092, HD 87015, and HD 17081 we determined the mass by comparing the position of the stars in the sHRD with evolutionary tracks by Ekström et al. (2012) and then calculated the additional parameters. In the case of the fast-rotating objects HD 149757 and HD 93827 we first calculated their radius from the measured parallax distance d_{Gaia} and the V magnitude corrected for extinction

$$\log(R/R_\odot) \approx 7.398 - 0.2\cdot(V - R_V\cdot E(B-V) - m_{\rm syn}) + \log(d/{\rm pc}), \quad (3)$$

where $m_{\rm syn} = -2.5\int F(\lambda)\cdot T(\lambda)\,{\rm d}\lambda + zp$ is a synthetic magnitude calculated from the theoretical astrophysical flux $F(\lambda)$, the filter response function $T(\lambda)$, and the zero-point zp of the filter. Then we corrected our derived $\log(g)$ values for centrifugal acceleration using the equation by Repolust et al. (2004)

$$g_{\rm true} \approx g + \frac{(v\sin i)^2}{R} \quad (4)$$

and determined the mass in the sHRD with the corrected surface gravity. For HD 149757 we obtain $\log(g_{\rm true}) = 3.91\pm0.07$ and for HD 93827 $\log(g_{\rm true}) = 3.55\pm0.07$ (the centrifugal acceleration is negligible for the other sample stars). The exceptional case of HD 149757 is discussed in more detail further below. We note that the derived spectroscopic distance for both objects is not an independent distance measurement since we used the radius calculated from the parallax distance.

As our analysis results for the benchmark stars agree with those derived earlier in the literature, we refer for the discussion of their fundamental stellar parameters to Nieva & Przybilla (2014), Weßmayer et al. (2022, 2023) and Aschenbrenner et al. (2023). The combined radial-velocity and light curve analysis feasible for DEBs allows highly accurate and precise fundamental parameters to be derived; we therefore refer to the studies of Garcia et al. (2014) for the data on V578 Mon and Albrecht et al. (2014) for CV Vel.

HD 149757 (ζ Oph). The very high rotational speed of at least ~90% of the critical velocity makes ζ Oph one of the fastest rotating OB stars in the Milky Way known at present. Together with its runaway nature, it appears to be the product of binary interaction (Renzo & Götberg 2021), where the mass overflow led to the spin-up and the supernova explosion of its companion made it speed away from its birth place. A little extra discussion is therefore in place when deriving its fundamental parameters.

The distance of ζ Oph is the crucial factor. Three reasonable parallax measurements give values of 140^{+16}_{-12} pc (Hipparcos, ESA 1997), 112^{+3}_{-2} pc (new reduction of the Hipparcos data, van Leeuwen 2007), and 135^{+12}_{-9} pc (*Gaia* EDR3, Bailer-Jones et al. 2021). The first two measurements lead to an association of ζ Oph with two different pulsars as the products of a binary supernova explosion in the Upper Scorpius subgroup (Hoogerwerf et al. 2001) or the Upper Centaurus Lupus subgroup (Neuhäuser et al. 2020) of the Sco OB2 association. The short Hipparcos distance would result in a $\log L/L_\odot \approx 4.5$, comparable to the least luminous O9.7 V star in the sample of Aschenbrenner et al. (2023); the luminosity at the *Gaia* (and the long Hipparcos) distance, on the other hand, is comparable to those of the O9.2 IV stars in that work. We therefore adopted the *Gaia* distance, despite a poor RUWE value of 4.489 (the star is brighter than the original bright star limit of *Gaia*, and we speculate that variations of the star's photocentre due to the strong non-radial pulsations may also be an issue, with the parallax error of 0.6596 mas being similar in size than the measured angular diameter of the star, 0.462–0.540 mas, Gordon et al. 2018). The radius follows from Eq. (3), which is in good agreement with the radius value derived from the angular diameter. Our mass determination has to be viewed with more care, as we employed tracks for single star evolution. Ideally, a tailored binary evolution model similar to that of Renzo & Götberg (2021) would need to be computed, meeting our observational constraints. But the differences between single and binary star evolution at the position of ζ Oph in the HRD (their Fig. 1) are not large (they will become important during further evolution), such that systematic errors can be expected to remain small. However, the value for the evolutionary age from our approach is only a lower limit. Finally, we note that the observed helium and CNO abundances are a consequence of the accretion of nuclear-processed material from the former companion star and subsequent thermohaline mixing because of the inverted mean molecular weight gradient near the surface.

5. Summary and outlook

In this paper, we present the first results from using Saturn, a programme we developed to fit spectra of single and multiple OB-type stars. We used neural networks to emulate model

spectra for a wide range of atmospheric parameters and account for lines of hydrogen, helium, and ten metals. Broadening with instrumental, rotational, and radial-tangential macroturbulence profiles is handled separately. The neural networks were trained on a dataset we calculated with a hybrid non-LTE approach based on the ATLAS, DETAIL, and SURFACE codes, and which cover a wavelength range from 3000 to 10 500 Å.

We first tested SATURN by analysing five, apparently slowly rotating, single stars. Previous literature data on atmospheric parameters and element abundances were reproduced. We also analysed a single epoch spectrum of the DEB HD 259135 (V578 Mon), and reproduced values from the literature derived from independent measurements of the radial-velocity and light curves. Of particular importance is the ability to match the observed spectra very closely at very high S/N, both in terms of completeness of the involved line list and in the match of the strengths and shapes of the spectral features.

As further applications, we used SATURN to analyse an additional DEB and five single stars, among others the rapidly rotating star HD 149757 (ζ Oph), and determined their atmospheric parameters and their chemical composition with high precision. This demonstrates the strength of SATURN to also analyse fast-rotating stars with relative ease, where blended spectral lines dominate the spectra, putting the aforementioned completeness of the line lists to a test.

For the analysis of the objects we used available high-quality, high-resolution spectra, at $R \geq 40\,000$. This opens up the possibility of analysing similar data for OB-type stars, be it new observations taken with state-of-the-art instrumentation, or by taking advantage of the vast existing telescope archives. A huge incentive for the development of SATURN was to have a tool at hand to efficiently analyse the coming flood of data from spectroscopic facilities such as WEAVE and 4MOST, which will provide spectra for tens of thousands of OB-type stars with resolutions from $R \approx 4000$ to 20 000. By analysing low-resolution XSHOOTER spectra of the benchmark star HD 35299, we could also show the capability of SATURN to perform at lower spectral resolution, reproducing atmospheric parameters and chemical abundances at similar quality. However, the number of accessible chemical species is reduced because of increased instrumental broadening and can be expected to be further reduced at higher rotation velocities and for decreasing S/N, which will also increase the uncertainties of the atmospheric parameters.

The analysis framework realised in SATURN can, of course, be extended to other types of stars. One direction could be subluminous O and B stars (e.g. Heber 2016), ideal objects for hydrostatic analyses with ADS even to higher effective temperatures than covered here because of their much higher gravities, $\log(g) \approx 5$–6, and their negligible winds. Some first steps in this direction have already been taken (e.g. Przybilla et al. 2006b; Schaffenroth et al. 2021). Atomic diffusion in their very stable atmospheres is an issue, though, which is noticeable through widely varying helium and metal abundances.

Extensions towards the modelling of cooler A-type stars are also aspired, to cover the full scope of existing investigations such as by Xiang et al. (2022) or Sun (2025). Currently, we use a mixture of non-LTE and LTE spectrum synthesis with ADS to cope with the much wider range of chemical species present in the spectra (e.g. Przybilla et al. 2006a, 2017). Clearly, a substantial extension of the non-LTE model atom database would be desirable. However, a word of caution is in order. The A-type stars with surface gravities as typical for the main sequence comprise to a considerable percentage objects of non-standard abundances, such as Am- and Ap-type stars, λ Boo stars, metal-poor blue horizontal branch stars and blue stragglers. Slowly rotating A-type and late B-type stars pose in their entirety the probably most difficult star classes to be analysed because of their diversity, bringing pre-calculated models sooner or later to their limit.

In any case, SATURN will provide a highly useful means for an efficient analysis of stellar spectra beyond the immediate applications presented here. We plan a public release of SATURN in the future, once the ongoing model development for ADS is completed.

Data availability

Most optical spectra used in this paper are publicly available and can be downloaded from the ESO Science Portal and the CFHT Science Archive. Observed IUE spectrophotometry and Gaia XP spectra are available from the respective archives. Photometric measurements used can be accessed using the VizieR Catalogue Service. The model SEDs, model spectra, and normalised spectra shown in the plots are available on Zenodo and can be accessed via the following link DOI: 10.5281/zenodo.19387709. Missing data, model fits, or code outputs are available upon reasonable request.

Acknowledgements. The authors thank M.A. Urbaneja for valuable discussions and A. Ebenbichler for the provision of his DIB linelist. P.A. acknowledges support of this work by grant of a Ph.D. stipend from the Vice Rectorate for Research of the University of Innsbruck. The present work uses observations collected at the Centro Astronómico Hispano Alemán at Calar Alto (CAHA), operated jointly by the Max-Planck Institut für Astronomie and the Instituto de Astrofísica de Andalucía (CSIC), proposal H2005-2.2-016, and observations collected at the European Southern Observatory under ESO programme 091.C-0713(A). Based on data obtained from the ESO Science Archive Facility with DOIs: https://doi.org/10.18727/archive/24 and https://doi.org/10.18727/archive/33. It also employs observations made with the Nordic Optical Telescope, owned in collaboration by the University of Turku and Aarhus University, and operated jointly by Aarhus University, the University of Turku, and the University of Oslo, representing Denmark, Finland and Norway, the University of Iceland, and Stockholm University at the Observatorio del Roque de los Muchachos, La Palma, Spain, of the Instituto de Astrofisica de Canarias. The NOT data were obtained under programme ID P41-027. This research used the facilities of the Canadian Astronomy Data Centre operated by the National Research Council of Canada with the support of the Canadian Space Agency.

References

Adelman, S. J., Pintado, O. I., Nieva, M. F., Rayle, K. E., & Sanders, Jr., S. E. 2002, A&A, 392, 1031
Albrecht, S., Winn, J. N., Torres, G., et al. 2014, ApJ, 785, 83
Araya, I., Curé, M., Machuca, N., et al. 2025, A&A, 704, A77
Aschenbrenner, P., & Przybilla, N. 2024, A&A, 691, A361
Aschenbrenner, P., Przybilla, N., & Butler, K. 2023, A&A, 671, A36
Aschenbrenner, P., Butler, K., & Przybilla, N. 2025, A&A, 698, A164
Bailer-Jones, C. A. L., Rybizki, J., Fouesneau, M., Demleitner, M., & Andrae, R. 2021, AJ, 161, 147
Balona, L. A., & Ozuyar, D. 2020, MNRAS, 493, 5871
Bätz, J., Mugrauer, M., Michel, K. U., et al. 2026, Astron. Nachr., 347, e70055
Beauchamp, A., Wesemael, F., & Bergeron, P. 1997, ApJS, 108, 559
Becker, S. R. 1998, ASP Conf. Ser., 131, 137
Blomme, R., Daflon, S., Gebran, M., et al. 2022, A&A, 661, A120
Butler, K., & Giddings, J. R. 1985, Newsletter of Analysis of Astronomical Spectra, 9 (London: University of London)
Castro, N., Crowther, P. A., Evans, C. J., et al. 2018, A&A, 614, A147
Chini, R., Hoffmeister, V. H., Nasseri, A., Stahl, O., & Zinnecker, H. 2012, MNRAS, 424, 1925
Cutri, R. M., Skrutskie, M. F., van Dyk, S., et al. 2003, VizieR Online Data Catalog: II/246
Cutri, R. M., Wright, E. L., Conrow, T., et al. 2021, VizieR Online Data Catalog: II/328
de Burgos, A., Simón-Díaz, S., Urbaneja, M. A., & Puls, J. 2024, A&A, 687, A228
de Jong, R. S., Agertz, O., Berbel, A. A., et al. 2019, The Messenger, 175, 3
Dimitrijevic, M. S., & Sahal-Brechot, S. 1990, A&AS, 82, 519

Ekström, S., Georgy, C., Eggenberger, P., et al. 2012, A&A, 537, A146
ESA, ed. 1997, ESA SP, 1200
Evans, C. J., Smartt, S. J., Lee, J. K., et al. 2005, A&A, 437, 467
Evans, C. J., Taylor, W. D., Hénault-Brunet, V., et al. 2011, A&A, 530, A108
Evans, C. J., Castro, N., Gonzalez, O. A., et al. 2019, A&A, 622, A129
Fitzpatrick, E. L. 1999, PASP, 111, 63
Flores, R. M., Corral, L. J., Fierro-Santillán, C. R., & Navarro, S. G. 2023, Astron. Comput., 45, 100760
Fossati, L., Ryabchikova, T., Bagnulo, S., et al. 2009, A&A, 503, 945
Fraser, M., Dufton, P. L., Hunter, I., & Ryans, R. S. I. 2010, MNRAS, 404, 1306
Frémat, Y., Zorec, J., Hubert, A.-M., & Floquet, M. 2005, A&A, 440, 305
Froese Fischer, C., & Tachiev, G. 2004, At. Data Nucl. Data Tables, 87, 1
Froese Fischer, C., Tachiev, G., & Irimia, A. 2006, At. Data Nucl. Data Tables, 92, 607
Gaia Collaboration (Prusti, T., et al.) 2016, A&A, 595, A1
Gaia Collaboration (Brown, A. G. A., et al.) 2021, A&A, 649, A1
Gaia Collaboration (Vallenari, A., et al.) 2023, A&A, 674, A1
Garcia, E. V., Stassun, K. G., Pavlovski, K., et al. 2014, AJ, 148, 39
Gebruers, S., Tkachenko, A., Bowman, D. M., et al. 2022, A&A, 665, A36
Gerasimovič, B. P. 1929, MNRAS, 89, 272
Giddings, J. R. 1981, PhD thesis, University of London, UK
González, J. F., Briquet, M., Przybilla, N., et al. 2019, A&A, 626, A94
González-Torà, G., Urbaneja, M. A., Przybilla, N., et al. 2022, A&A, 658, A117
Gordon, K. D., Gies, D. R., Schaefer, G. H., et al. 2018, ApJ, 869, 37
Gräfener, G., Koesterke, L., & Hamann, W. R. 2002, A&A, 387, 244
Gray, D. F. 2005, The Observation and Analysis of Stellar Photospheres, 3rd edn. (Cambridge: Cambridge University Press)
Hamann, W. R., & Gräfener, G. 2003, A&A, 410, 993
Heber, U. 2016, PASP, 128, 082001
Hillier, D. J., & Miller, D. L. 1998, ApJ, 496, 407
Hoogerwerf, R., de Bruijne, J. H. J., & de Zeeuw, P. T. 2001, A&A, 365, 49
Hornik, K., Stinchcombe, M., & White, H. 1989, Neural Netw., 2, 359
Huang, W., Gies, D. R., & McSwain, M. V. 2010, ApJ, 722, 605
Hubeny, I. 1988, Comput. Phys. Commun., 52, 103
Hubeny, I., & Mihalas, D. 2015, Theory of Stellar Atmospheres (Princeton: Princeton University Press)
Hubeny, I., Hummer, D. G., & Lanz, T. 1994, A&A, 282, 151
Hummer, D. G., & Mihalas, D. 1988, ApJ, 331, 794
Hutter, D. J., Tycner, C., Zavala, R. T., et al. 2021, ApJS, 257, 69
Irrgang, A. 2014, PhD thesis, University of Erlangen-Nuremberg, Germany
Irrgang, A., Przybilla, N., Heber, U., Nieva, M. F., & Schuh, S. 2010, ApJ, 711, 138
Irrgang, A., Przybilla, N., Heber, U., et al. 2014, A&A, 565, A63
Irrgang, A., Przybilla, N., & Meynet, G. 2022, Nat. Astron., 6, 1414
Jin, S., Trager, S. C., Dalton, G. B., et al. 2024, MNRAS, 530, 2688
Kalita, A. J., Bowman, D. M., Abdul-Masih, M., & Simón-Díaz, S. 2025, A&A, 703, A2
Kaufer, A., Stahl, O., Tubbesing, S., et al. 1999, The Messenger, 95, 8
Kilian, J. 1994, A&A, 282, 867
Kingma, D. P., & Ba, J. 2017, arXiv e-prints [arXiv:1412.6980]
Kovalev, M., & Straumit, I. 2023, MNRAS, 523, 3741
Kovalev, M., Bergemann, M., Ting, Y.-S., & Rix, H.-W. 2019, A&A, 628, A54
Kovalev, M., Chen, X., & Han, Z. 2022, MNRAS, 517, 356
Krtička, J., & Kubát, J. 2017, A&A, 606, A31
Kudritzki, R. P., Urbaneja, M. A., Gazak, Z., et al. 2012, ApJ, 747, 15
Kudritzki, R. P., Urbaneja, M. A., Bresolin, F., Hosek, M. W., & Przybilla, N. 2014, ApJ, 788, 56
Kurucz, R. 1993, CD-ROM (Cambridge, Mass.: SAO), 13
Kurucz, R. L. 1996, ASP Conf. Ser., 108, 160
Lacy, C. H. S., Fekel, F. C., Mathieu, R. D., et al. 1997, AJ, 113, 1088
Langer, N., & Kudritzki, R. P. 2014, A&A, 564, A52
Liu, C., Fu, J., Shi, J., et al. 2020, arXiv e-prints [arXiv:2005.07210]
Lyubimkov, L. S., Rachkovskaya, T. M., Rostopchin, S. I., & Lambert, D. L. 2002, MNRAS, 333, 9
Maeder, A., Przybilla, N., Nieva, M. F., et al. 2014, A&A, 565, A39
Manset, N., & Donati, J.-F. 2003, Proc. SPIE, 4843, 425
Mashonkina, L., Ryabchikova, T., Alexeeva, S., Sitnova, T., & Zatsarinny, O. 2020, MNRAS, 499, 3706
Mason, B. D., Wycoff, G. L., Hartkopf, W. I., Douglass, G. G., & Worley, C. E. 2001, AJ, 122, 3466
Mayor, M., Pepe, F., Queloz, D., et al. 2003, The Messenger, 114, 20
Maza, N. L., Nieva, M. F., & Przybilla, N. 2014, A&A, 572, A112
Mermilliod, J. C. 1997, VizieR Online Data Catalog: II/168
Metropolis, N., Rosenbluth, A. W., Rosenbluth, M. N., Teller, A. H., & Teller, E. 1953, J. Chem. Phys., 21, 1087
Michaud, G. 1970, ApJ, 160, 641
Mokiem, M. R., de Koter, A., Puls, J., et al. 2005, A&A, 441, 711
Morel, T., & Butler, K. 2008, A&A, 487, 307
Morel, T., Butler, K., Aerts, C., Neiner, C., & Briquet, M. 2006, A&A, 457, 651
Morel, T., Blazère, A., Semaan, T., et al. 2022, A&A, 665, A108
Morrell, N., & Levato, H. 1991, ApJS, 75, 965
Najarro, F., Hillier, D. J., Puls, J., Lanz, T., & Martins, F. 2006, A&A, 456, 659
Ness, M., Hogg, D. W., Rix, H.-W., Ho, A. Y. Q., & Zasowski, G. 2015, ApJ, 808, 16
Neuhäuser, R., Gießler, F., & Hambaryan, V. V. 2020, MNRAS, 498, 899
Nieva, M. F., & Przybilla, N. 2006, ApJ, 639, L39
Nieva, M. F., & Przybilla, N. 2007, A&A, 467, 295
Nieva, M. F., & Przybilla, N. 2008, A&A, 481, 199
Nieva, M. F., & Przybilla, N. 2012, A&A, 539, A143
Nieva, M. F., & Przybilla, N. 2014, A&A, 566, A7
Paszke, A., Gross, S., Massa, F., et al. 2019, arXiv e-prints [arXiv:1912.01703]
Pauldrach, A. W. A., Hoffmann, T. L., & Lennon, M. 2001, A&A, 375, 161
Pavlovski, K., Southworth, J., & Tamajo, E. 2018, MNRAS, 481, 3129
Pavlovski, K., Southworth, J., Tkachenko, A., Van Reeth, T., & Tamajo, E. 2023, A&A, 671, A139
Payne-Gaposchkin, C. H. 1925, PhD thesis, Radcliffe College, Cambridge, MA, USA
Pfeiffer, M. J., Frank, C., Baumueller, D., Fuhrmann, K., & Gehren, T. 1998, A&AS, 130, 381
Przybilla, N. 2005, A&A, 443, 293
Przybilla, N., & Butler, K. 2001, A&A, 379, 955
Przybilla, N., & Butler, K. 2004, ApJ, 609, 1181
Przybilla, N., Butler, K., Becker, S. R., Kudritzki, R. P., & Venn, K. A. 2000, A&A, 359, 1085
Przybilla, N., Butler, K., Becker, S. R., & Kudritzki, R. P. 2001a, A&A, 369, 1009
Przybilla, N., Butler, K., & Kudritzki, R. P. 2001b, A&A, 379, 936
Przybilla, N., Butler, K., Becker, S. R., & Kudritzki, R. P. 2006a, A&A, 445, 1099
Przybilla, N., Nieva, M. F., & Edelmann, H. 2006b, Balt. Astron., 15, 107
Przybilla, N., Firnstein, M., Nieva, M. F., Meynet, G., & Maeder, A. 2010, A&A, 517, A38
Przybilla, N., Nieva, M. F., Irrgang, A., & Butler, K. 2013, EAS Publ. Ser., 63, 13
Przybilla, N., Aschenbrenner, P., & Buder, S. 2017, A&A, 604, L9
Przybilla, N., Fossati, L., & Jeffery, C. S. 2021, A&A, 654, A119
Puls, J., Urbaneja, M. A., Venero, R., et al. 2005, A&A, 435, 669
Puls, J., Najarro, F., Sundqvist, J. O., & Sen, K. 2020, A&A, 642, A172
Renzo, M., & Götberg, Y. 2021, ApJ, 923, 277
Repolust, T., Puls, J., & Herrero, A. 2004, A&A, 415, 349
Rivinius, T., Carciofi, A. C., & Martayan, C. 2013, A&A Rev., 21, 69
Różański, T., Ting, Y.-S., & Jabłońska, M. 2025, ApJ, 980, 66
Rybicki, G. B., & Hummer, D. G. 1991, A&A, 245, 171
Sana, H., de Mink, S. E., de Koter, A., et al. 2012, Science, 337, 444
Sander, A., Shenar, T., Hainich, R., et al. 2015, A&A, 577, A13
Schaffenroth, V., Casewell, S. L., Schneider, D., et al. 2021, MNRAS, 501, 3847
Schoening, T., & Butler, K. 1989, A&AS, 78, 51
Sigut, T. A. A., McGill, M. A., & Jones, C. E. 2009, ApJ, 699, 1973
Simón-Díaz, S., Pérez Prieto, J. A., Holgado, G., de Burgos, A., & Iacob Team 2020, in XIV.0 Scientific Meeting (virtual) of the Spanish Astronomical Society, 187
Smith, K. C. 1996, Ap&SS, 237, 77
Straumit, I., Tkachenko, A., Gebruers, S., et al. 2022, AJ, 163, 236
Sun, W. 2025, A&A, 698, A300
Tamajo, E., Pavlovski, K., & Southworth, J. 2011, A&A, 526, A76
Telting, J. H., Avila, G., Buchhave, L., et al. 2014, Astron. Nachr., 335, 41
Ting, Y.-S., Conroy, C., Rix, H.-W., & Cargile, P. 2019, ApJ, 879, 69
Tokovinin, A., Mason, B. D., & Hartkopf, W. I. 2010, AJ, 139, 743
Tremblay, P. E., & Bergeron, P. 2009, ApJ, 696, 1755
Turner, N. H., ten Brummelaar, T. A., Roberts, L. C., et al. 2008, AJ, 136, 554
Urbaneja, M. A. 2026, A&A, 707, A249
Urbaneja, M. A., Kudritzki, R. P., Bresolin, F., et al. 2008, ApJ, 684, 118
Urbaneja, M. A., Kudritzki, R. P., Gieren, W., et al. 2017, AJ, 154, 102
van Leeuwen, F. 2007, A&A, 474, 653
Vernet, J., Dekker, H., D'Odorico, S., et al. 2011, A&A, 536, A105
Vink, J. S., Mehner, A., Crowther, P. A., et al. 2023, A&A, 675, A154
Vrancken, M., Butler, K., & Becker, S. R. 1996, A&A, 311, 661
Walborn, N. R. 1976, ApJ, 205, 419
Walker, G. A. H., Kuschnig, R., Matthews, J. M., et al. 2005, ApJ, 623, L145
Weßmayer, D., Przybilla, N., & Butler, K. 2022, A&A, 668, A92
Weßmayer, D., Przybilla, N., Ebenbichler, A., Aschenbrenner, P., & Butler, K. 2023, A&A, 677, A175
Xiang, M., Rix, H.-W., Ting, Y.-S., et al. 2022, A&A, 662, A66
Yakut, K., Aerts, C., & Morel, T. 2007, A&A, 467, 647
Zboril, M., North, P., Glagolevskij, Y. V., & Betrix, F. 1997, A&A, 324, 949

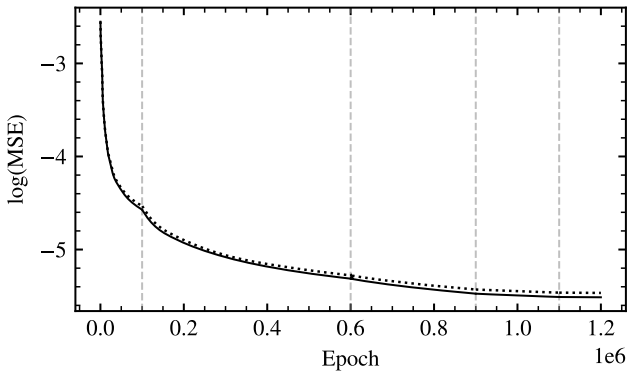

Fig. A.1. Mean squared error as a function of training epoch. The solid line is the MSE for the training data and the dotted line for the test data. The dashed vertical lines mark the epochs where the learning rate was reduced.

Appendix A: Neural network training

For the training of the neural networks, we used 90% of the calculated models, the remaining 10% were used for testing. We trained the neural networks by minimising the mean squared error (MSE) over all n training models with m wavelength points each

$$\mathrm{MSE} = \frac{1}{n}\sum_{i=1}^{n}\frac{1}{m}\sum_{j=1}^{m}\left(y_i(\lambda_j) - f_i(\lambda_j)\right)^2 , \tag{A.1}$$

where $y_i(\lambda_j)$ is the model flux and $f_i(\lambda_j)$ the predicted flux at wavelength point λ_j. We used the Adam optimiser (Kingma & Ba 2017) to minimise the MSE, with an initial learning rate of $1E{-}2$. After a fixed number of training epochs (1E5, 5E5, 3E5, 2E5) we reduced the learning rate to one tenth of the previous value. After 1.2 million epochs in total, we stopped the training. The behaviour of the MSE over the training epochs is shown in Fig. A.1. The MSE of the test and training data follow exactly the same trend, indicating that no over-fitting of the training data occurred. The training of one neural network (i.e. a network as described in the main text with 14 input neurons and 7500 output neurons) with 4500 training models took less than 45 min on a consumer graphics processing unit.

Appendix B: Microturbulence

The usual approach – adjusting the microturbulence so that the fitted abundance of individual lines of a single element ε_p becomes independent of the equivalent width W_p – assumes a linear relation

$$\varepsilon_p = k(\xi)\cdot W_p + d(\xi) + \sigma_{\varepsilon_p} . \tag{B.1}$$

In Eq. (B.1) p is an index for the different spectral lines, $k(\xi)$ the slope as a function of microturbulence, $d(\xi)$ the intersection and $\sigma_{\varepsilon_p} \sim \mathcal{N}(0, \sigma_\varepsilon^2)$ the assumed normal distributed uncertainties of the individual line abundances. Calculating the expected variance $\mathrm{E}[(\varepsilon_p - \mathrm{E}[\varepsilon_p])^2]$ of the individual line abundances ε_p, one finds

$$\mathrm{E}[(\varepsilon_p - \mathrm{E}[\varepsilon_p])^2] = \sigma_\varepsilon^2 + k(\xi)^2\sigma_W^2 , \tag{B.2}$$

where σ_W^2 is the variance of the distribution of equivalent widths. For a finite and non-zero σ_W^2, the minimum of Eq. (B.2) is at $k(\xi{=}\xi_0) = 0$, proving the equivalence of minimising the variance of individual line abundances to the approach of strength-independent line abundances.

To determine the microturbulence of the stars analysed in this paper, we use Eq. (2) to fit multiple lines of one element with ξ and the abundance ε as free parameters. To estimate the most likely parameters ξ and ε, we assume the true parameters are ξ_0 and ε_0 and that each line is fitted by the true microturbulence value ξ_0 and the abundance ε_p (linearisation of Eq. (B.1))

$$\varepsilon_p \approx \varepsilon_0 + k\cdot(\xi - \xi_0)\cdot W_p + \sigma_{\varepsilon_p} . \tag{B.3}$$

Also linearising the model flux for the p-th spectral line and assuming constant derivatives at all wavelength points one obtains

$$\begin{aligned} f(\xi,\,\varepsilon)_{\lambda_i,\mathrm{mod}} &\approx f(\xi_0,\,\varepsilon_p)_{\lambda_i,\mathrm{mod}} \\ &\quad + (\xi - \xi_0)\left.\frac{\partial f(\xi,\,\varepsilon)_{\lambda_i,\mathrm{mod}}}{\partial \xi}\right|_{\xi=\xi_0} \\ &\quad + (\varepsilon - \varepsilon_p)\left.\frac{\partial f(\xi,\,\varepsilon)_{\lambda_i,\mathrm{mod}}}{\partial \varepsilon}\right|_{\varepsilon=\varepsilon_p} \\ &\approx \bar{f}_{\lambda_i,\mathrm{mod}} + (\xi - \xi_0)\cdot\Delta_\xi + (\varepsilon - \varepsilon_p)\cdot\Delta_\varepsilon . \end{aligned} \tag{B.4}$$

Inserting Eq. (B.4) in Eq. (2) and assuming constant uncertainties ($\sigma^2_{\lambda_i,\mathrm{stat}} + \sigma^2_{\lambda_i,\mathrm{sys}} \approx \mathrm{const.}$) the gradient of the negative log-likelihood can be calculated. Setting the gradient to zero we find

$$\xi = \xi_0 + \frac{\frac{1}{|p|}\cdot\sum_p W_p\sigma_{\varepsilon_p}}{k\cdot\left(\left(\frac{1}{|p|}\sum_p W_p\right)^2 - \frac{1}{|p|}\sum_p W_p^2\right)}$$

$$\varepsilon = \varepsilon_0 + (\xi - \xi_0)\cdot\left(\frac{k}{|p|}\sum_p W_p - \frac{\Delta_\xi}{\Delta_\varepsilon}\right),$$

where $|p| = \sum_p 1$ is the number of spectral lines used for fitting. Finally, if the individual abundance uncertainties σ_{ε_p} are independent of the equivalent widths W_p, we expect $\sum_i W_i\sigma_i = 0$ since $\mathrm{E}[W_p\sigma_{\varepsilon_p}] = \mathrm{E}[W_p]\cdot\mathrm{E}[\sigma_{\varepsilon_p}] = 0$ and consequently the parameters maximising the likelihood function are the true parameters $\xi = \xi_0$ and $\varepsilon = \varepsilon_0$.

Appendix C: SED fits

To constrain the interstellar extinction to the binary systems, we calculated the theoretical SED by using the sum of the ATLAS9 model fluxes of the two individual stars, scaled by the squared radii. The model was fitted to observed Johnson UBV (Mermilliod 1997), 2MASS JHK (Cutri et al. 2003), and WISE $W1$ to $W4$ (Cutri et al. 2021) photometry. In the case of HD 77464 spectra taken with the International Ultraviolet Explorer (IUE) are available from the Mikulski Archive for Space Telescopes (MAST[4]). To account for interstellar extinction, we used the reddening law of Fitzpatrick (1999), parametrised by the colour excess $E(B-V)$ and the ratio of total-to-selective extinction, $R_V = A_V/E(B-V)$. From a least-squares fit we obtained $R_V = 2.95\pm0.04$ and $E(B-V) = 0.474\pm0.006$ for HD 259135. For HD 77464 we set $R_V = 3.1$ and obtained $E(B-V) = 0.034\pm0.010$. The best fit for both systems is shown in Fig. C.1.

We also determined interstellar extinction towards the new single targets (Sect. 4.2). Information on the IUE

[4] https://archive.stsci.edu/iue/

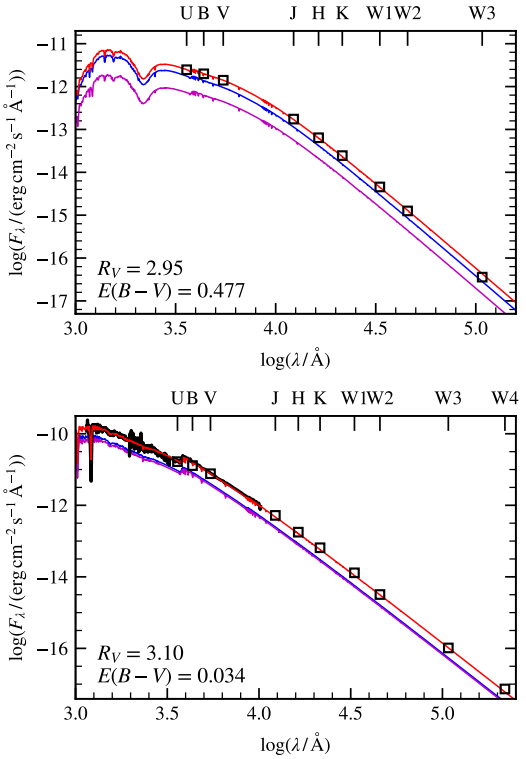

Fig. C.1. Spectral energy distribution fits of the reddened combined ATLAS9 model fluxes (red) to photometric measurements (black squares) and observed IUE spectrophotometry and Gaia XP spectra (Gaia Collaboration 2023) (black line), if available. The contributions of the primary and secondary are shown in blue and magenta, respectively. Top panel: SED fit for HD 259135 (V578 Mon); bottom panel: SED fit for HD 77464 (CV Vel).

spectrophotometric data that was employed for the comparison of the observed SED with the model fluxes is summarised in Table C.1, supplemented by Johnson, 2MASS, and WISE photometry as in the case of the binaries.

Appendix D: Spectrum fits

We show a comparison between the observed spectrum from 3950Å-4750Å and the global best-fitting model, created with the neural networks, for HD 259135 (V578 Mon) in Fig. D.1, for HD 149757 (ζ Oph) in Fig. D.2, for HD 93827 in Fig. D.3, and for HD 77464 (CV Vel) in Fig. D.4. Except for the latter, the objects show more or less prominent diffuse interstellar bands (DIBs). In addition, interstellar lines such as the Ca II H and K lines are also present. We note the high quality of the fits at the very high S/N of the observed spectra, which implies overall completeness of the line list, correctness of oscillator strengths, proper determination of atmospheric parameters, and accurate and precise determination of level populations. The remaining discrepancies can best be seen in the residuals. The largest differences arise from the DIBs and the interstellar lines, which are not modelled. Inherent to the models are inaccuracies due to the oscillator strengths, which, to a good part, are responsible for the line-to-line abundance scatter. Uncertainties of less than 10-20% should be typical for the oscillator strengths of many of the metal lines investigated here, but some may reach 50%, as reflected by the quality markers assigned in the data collection of the National Institute of Standards and Technology[5]. In the case of HD 149757, additional deviations stem from pulsations of the star, which are not part of the modelling.

[5] https://www.nist.gov/pml/atomic-spectra-database

Table C.1. IUE spectrophotometry used in the present work.

Object	SW	Date	LW	Date
HD 149757	P32894	1988-02-10	P12637	1988-02-10
HD 93827	P48400	1993-08-16	P26160	1993-08-16
HD 112092	P21955	1984-01-07	P18239	1990-06-29
HD 87015	P21988	1984-01-11	P02597	1984-01-11
HD 17081	P16255	1982-02-04	R12501	1982-02-03
HD 77464	P50160	1994-03-03	P27555	1994-03-03

Appendix E: Tests with lower-resolution spectra

The availability of XSHOOTER data for our benchmark star HD 35299 facilitates testing of SATURN at spectral resolutions that are relevant for intermediate-resolution spectroscopy with XSHOOTER itself, as widely employed for OB-star observations in the XShootU survey (Vink et al. 2023), and for future large spectroscopic surveys with WEAVE and 4MOST. WEAVE will provide a wavelength coverage of about 3660 to 9590 Å (with some small gaps) in low-resolution mode ($R \approx 5000$) and three regions (4040-4650, 4730-5450 and 5950-6850 Å) at $R \approx 20\,000$ in the higher-resolution mode. 4MOST has similar characteristics, a wavelength coverage of about 3700 to 9500 Å in low-resolution mode ($R \approx 4000$ to 7700) and, again, three regions at about 3926–4355, 5160–5730 and 6100–6790 Å at $R \approx 18\,000$ to 21 000 in the higher-resolution mode. Many indicators for the stellar parameter and abundance determination will be accessible such that quantitative spectroscopy of OB-type stars will face only minor restrictions, mainly losing some redundancy.

The results of the stellar parameter determination from XSHOOTER spectra are compared to the solution from the analysis of the high-resolution FOCES data in Table E.1. The $R \approx 18\,000$ data cover the visual spectral range (VIS) from 5595 to 10240 Å, and the lower-resolution data the UV and blue range (UVB) from 3000 to 5595 Å. Excellent agreement of $T_{\rm eff}$, $\log(g)$, helium abundance and microturbulence within the error bars is found, with a slight trend towards the recovery of lower temperatures and lower gravity values at lower spectral resolution. The increased uncertainty in $\log(g)$ from the VIS analysis results from Hα being the only Balmer line available in that wavelength range, while the remainder of the Balmer series is covered in the UVB range. The combined rotational and macroturbulent velocity determination shows some small discrepancies, but one has to stress that for such an apparently slow rotator as HD 35299 the instrumental broadening dominates the line broadening at XSHOOTER resolution. One can expect that for faster rotators the agreement will be better.

The derived metal abundances for the different spectra are listed in Table E.2, again we find an excellent agreement. At lower spectral resolution, many of the weak spectral lines are no longer distinguishable from the continuum; an example in the case of HD 35299 are the phosphorus lines. For fast-rotating stars, even more spectral lines would be affected since they are already shallow due to rotational broadening. We further note that lines from some species are available in either the VIS or the UVB wavelength range, but not in both.

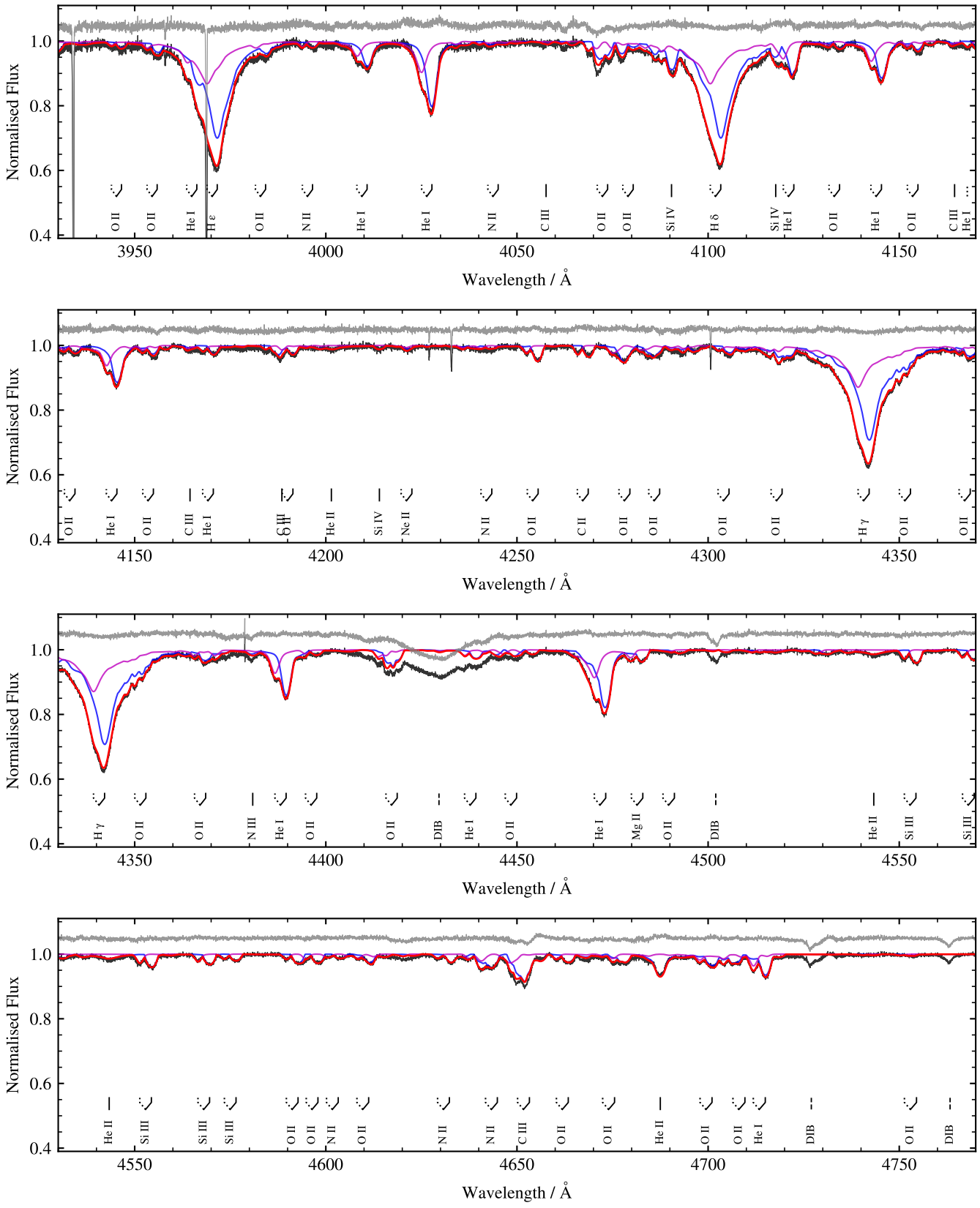

Fig. D.1. Comparison between the spectrum of the benchmark DEB HD 259135 (V578 Mon) in black and the global best-fitting model in red. The difference between observed and model flux is shown in grey at an offset of 1.05. The flux contributions of the primary and secondary star are shown in blue and magenta, respectively. The strongest spectral lines for the primary and secondary star are marked via solid and dotted lines, respectively. The DIBs are marked by dashed lines.

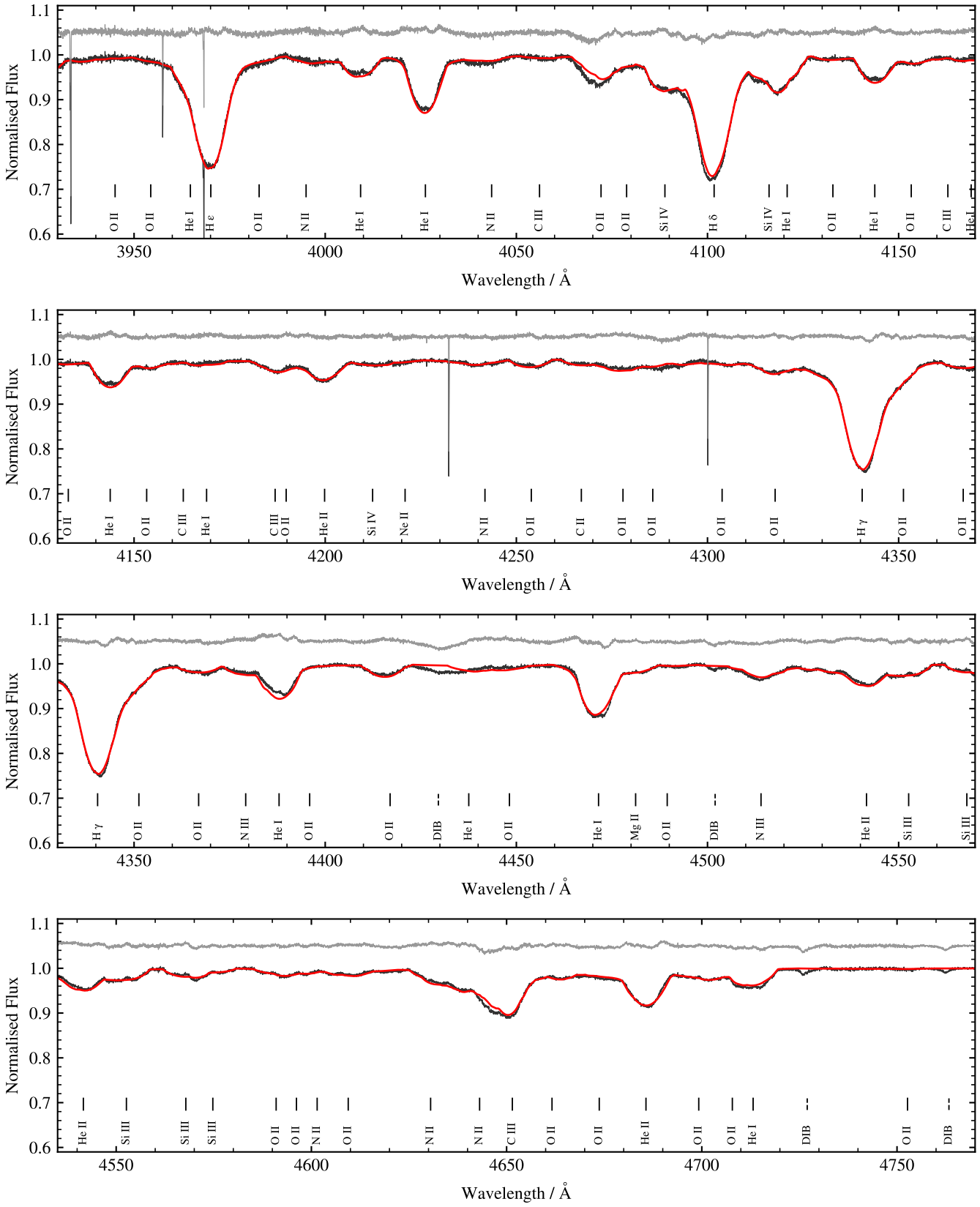

Fig. D.2. Comparison between the spectrum of the very fast rotator HD 149757 (ζ Oph) in black and the global best-fitting model in red. The difference between observed and model flux is shown in grey at an offset of 1.05. The strongest spectral lines are marked by solid lines, DIBs are marked by dashed lines.

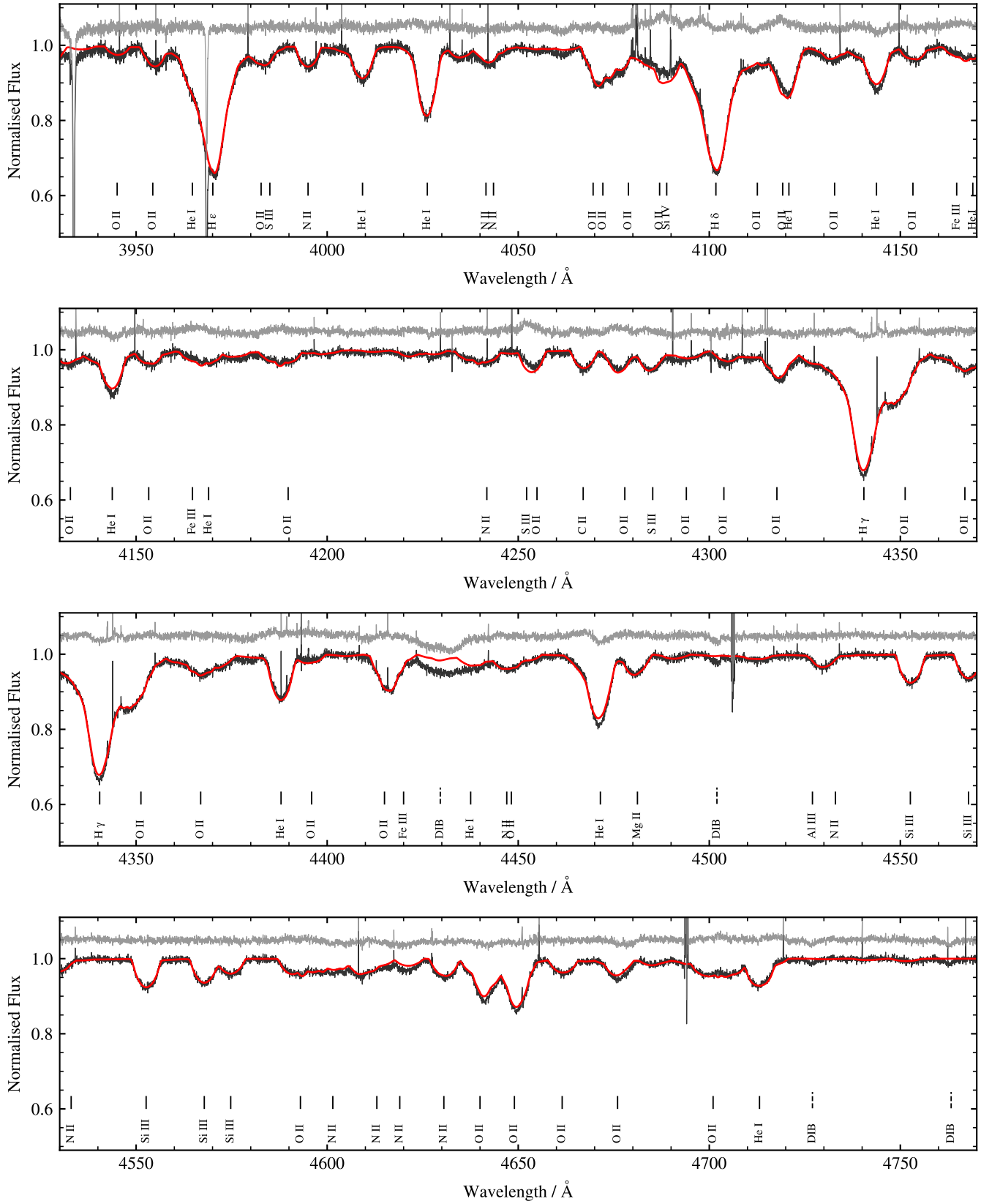

Fig. D.3. Comparison between the spectrum of the fast-rotating bright giant/supergiant HD 93827 in black and the global best-fitting model in red. The difference between observed and model flux is shown in grey at an offset of 1.05. The strongest spectral lines are marked via solid lines. The DIBs are indicated by dashed lines.

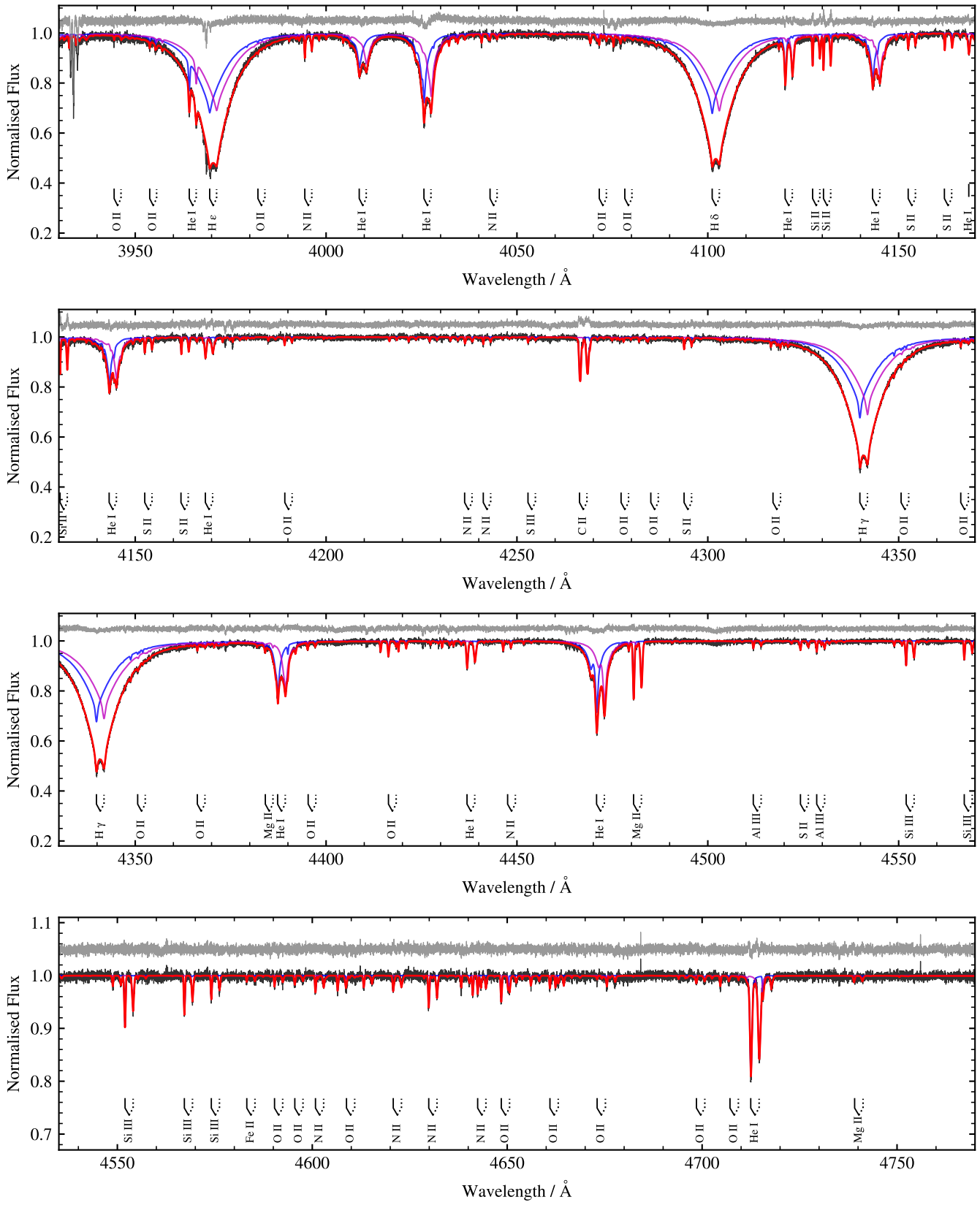

Fig. D.4. Comparison between the spectrum of the DEB HD 77464 (CV Vel) in black and the global best-fitting model in red. The difference between observed and model flux is shown in grey at an offset of 1.05. The flux contributions of the primary and secondary star are shown in blue and magenta, respectively. The strongest spectral lines for the primary and secondary star are marked via solid and dotted lines, respectively.

Table E.1. Comparison of stellar parameters derived at different spectral resolutions.

Object	Instrument	R	S/N	$T_{\rm eff}$	$\log(g)$	y	ξ	$v \sin i$	ζ
				K	(cgs)	by number		km s^{-1}	
HD 35299	FOCES	40 000	350	23391±521	4.19±0.06	0.092±0.002	0.5±0.6	1.4±0.8	8.3±0.2
	XSHOOTER	18 340	420	23230±453	4.19±0.09	0.090±0.003	0.8±0.6	3.8±2.5	7.8±1.6
	XSHOOTER	9861	640	23142±342	4.16±0.04	0.092±0.007	1.0±0.6	0.5±0.3	0.5±0.3
	XSHOOTER	5453	550	23292±479	4.17±0.06	0.099±0.007	1.3±0.7	1.8±1.3	1.7±1.3

Table E.2. Metal abundances $\varepsilon(X) = \log(X/\mathrm{H}) + 12$ (by number) for the star HD 35299, derived at different spectral resolutions.

R	C	N	O	Ne	Mg	Al	Si	P[a]	S	Fe
40 000	8.35±0.12	7.81±0.07	8.85±0.09	8.10±0.07	7.52±0.05	6.28±0.04	7.52±0.08	5.19±0.04	7.17±0.08	7.49±0.10
18 340	8.33±0.10	7.84±0.07	8.88±0.08	...	7.51	6.29±0.06	7.51±0.11	...	7.25±0.12	7.53±0.14
9861	8.31±0.06	7.77±0.06	8.83±0.06	8.06±0.05	7.51±0.06	6.35	7.59	...	7.19±0.12	7.52±0.11
5453	8.26±0.13	7.88±0.11	8.88±0.08	...	7.59	6.33±0.08	7.61±0.06	...	7.10±0.13	7.50±0.14